Atmos. Chem. Phys. manuscript:

Atmospheric Measurements at Mt. Tai - Part II: HONO Budget and Radical (RO$_x$ + NO$_3$) Chemistry in the Lower Boundary Layer

Chaoyang Xue[1, 2*], Can Ye[1, 6], Jörg Kleffmann[5], Wenjin Zhang[1], Xiaowei He[1, 9], Pengfei Liu[1, 3], Chenglong Zhang[1, 3], Xiaoxi Zhao[1, 9], Chengtang Liu[1, 3], Zhuobiao Ma[1], Junfeng Liu[1, 3], Jinhe Wang[7], Keding Lu[6], Valéry Catoire[2], Abdelwahid Mellouki[4, 8], Yujing Mu[1, 3*]

[1] Research Centre for Eco-Environmental Sciences, Chinese Academy of Sciences, Beijing 100085, China

[2] Laboratoire de Physique et Chimie de l'Environnement et de l'Espace (LPC2E), CNRS–Université Orléans–CNES, Cedex 2, Orléans 45071, France

[3] Centre for Excellence in Regional Atmospheric Environment, Institute of Urban Environment, Chinese Academy of Sciences, Xiamen 361021, China

[4] Institut de Combustion Aérothermique, Réactivité et Environnement, Centre National de la Recherche Scientifique (ICARE-CNRS), Cedex 2, Orléans 45071, France

[5] Physical and Theoretical Chemistry, University of Wuppertal, Gaußstrasse 20, 42119 Wuppertal, Germany

[6] State Key Joint Laboratory of Environment Simulation and Pollution Control, College of Environmental Sciences and Engineering, Peking University, Beijing, 100871, China

[7] School of Municipal and Environmental Engineering, Co-Innovation Centre for Green Building of Shandong Province, Shandong Jianzhu University, Jinan 250101, China

[8] Environmental Research Institute, Shandong University, Qingdao, Shandong 266237, China

[9] University of Chinese Academy of Sciences, Beijing 100049, China

Correspondence to:

Chaoyang Xue (chaoyang.xue@cnrs-orleans.fr; 86chaoyang.xue@gmail.com)

Yujing Mu (yjmu@rcees.ac.cn)

Abstract

In the summer of 2018, a comprehensive field campaign, with measurements on HONO and related parameters, was conducted at the foot (150 m a.s.l.) and the summit of Mt. Tai (1534 m a.s.l.) in the central North China Plain (NCP). With the implementation of a 0-D box model, the HONO budget with six additional sources and its role in radical chemistry at the foot station were explored. We found that the model default source, $NO + OH$, could only reproduce 13% of the observed HONO, leading to a strong unknown source strength of up to 3 ppbv h^{-1}. Among the additional sources, the NO_2 uptake on the ground surface dominated (~70%) night-time HONO formation, and its photo-enhanced reaction dominated (~80%) daytime HONO formation. Their contributions were sensitive to the mixing layer height (MLH) used for the parameterizations, highlighting the importance of a reasonable MLH for exploring ground-level HONO formation in 0-D models and the necessity of gradient measurements. A $\Delta HONO/\Delta NO_x$ ratio of 0.7% for direct emissions from vehicle exhaust was inferred and a new method to quantify its contribution to the observations was proposed and discussed. Aerosol-derived sources, including the NO_2 uptake on the aerosol surface and the particulate nitrate photolysis, did not lead to significant HONO formation, with their contributions lower than $NO + OH$.

HONO photolysis in the early morning initialized the daytime photochemistry at the foot station. It was also a substantial radical source throughout the daytime, with contributions higher than O_3 photolysis to OH initiation. Moreover, we found that OH dominated the atmospheric oxidizing capacity in the daytime, while modeled NO_3 appeared to be significant at night. Peaks of modeled NO_3 time series and average diurnal variation reached 22 and 9 pptv, respectively. NO_3 induced reactions contribute 18% of nitrate formation potential ($P(HNO_3)$) and 11% of the isoprene (C_5H_8) oxidation throughout the whole day. At night, NO_3 chemistry led to 51% and 44% of $P(HNO_3)$ or the C_5H_8 oxidation, respectively, implying that NO_3 chemistry could significantly affect night-time secondary organic and inorganic aerosol formation in this high-O_3 region. Considering the severe O_3 pollution in the NCP and the very limited NO_3 measurements, we suggest that besides direct measurements of HO_x and primary HO_x precursors (O_3, HONO, alkenes, etc.), NO_3 measurements should be conducted to understand the atmospheric oxidizing capacity and air pollution formation in this and similar regions.

1 Introduction

Numerous field campaigns coupled with model simulations have been conducted worldwide to understand the summertime atmospheric chemistry as it is linked to the regional air quality and global climate (Alicke et al., 2003; Elshorbany et al., 2012; Heard et al., 2004; Kanaya et al., 2009, 2013; Michoud et al., 2012; Ren et al., 2003; Rohrer and Berresheim, 2006; Tan et al., 2017; Travis et al., 2020). One of the key issues is the level and the production/loss paths of the atmospheric oxidizing capacity governed by radicals (OH, NO_3, etc.). This is also essential in converting primary to secondary pollutants and the removal of greenhouse gases (Lu et al., 2019; Seinfeld and Pandis, 2016).

On a global scale, OH controls atmospheric oxidation. As the detergent in the troposphere, OH can oxidize most trace gases, including inorganic (SO_2, NO_2, etc.) and organic compounds (VOCs, etc.), and determines the lifetime of greenhouse gases

(e.g., CH_4). Besides the fast conversion of HO_2 to OH (R-1) as part of the radical propagation cycle, primary OH (radical initiation) mainly originates from photolysis reactions, including O_3 ((R-2) to (R-4)), HONO (R-5), HCHO ((R-6) to (R-9), and (R-1)), and H_2O_2 (R-10), and the ozonolysis of alkenes (not shown in detail here). In particular, HONO photolysis is reported to be an important or even the major OH source in the lower atmosphere of polluted regions, with a contribution of 20 – 90% (Alicke et al., 2003; Elshorbany et al., 2009; Kleffmann et al., 2005; Platt et al., 1980; Slater et al., 2020; Whalley et al., 2021; Xue et al., 2020). However, this process still needs more global quantifications due to the incomplete understanding of HONO formation and its vertical distribution in the atmosphere (Kleffmann, 2007). A state-of-art summary of the reported HONO sources can be found in our recent study (Xue et al., 2020).

$$HO_2 + NO \rightarrow OH + NO_2 \tag{R-1}$$

$$O_3 + hv \rightarrow O(^1D) + O_2 \quad (\lambda{<}320 \text{ nm}) \tag{R-2}$$

$$O(^1D) + H_2O \rightarrow 2OH \tag{R-3}$$

$$O(^1D) + M \rightarrow O + M \quad (M{=}N_2 \text{ or } O_2) \tag{R-4}$$

$$HONO + hv \rightarrow NO + OH \quad (\lambda{<}400 \text{ nm}) \tag{R-5}$$

$$HCHO + hv \rightarrow H + HCO \quad (\lambda{<}340 \text{ nm}) \tag{R-6}$$

$$HCHO + hv \rightarrow H_2 + CO \quad (\lambda{<}365 \text{ nm}) \tag{R-7}$$

$$H + O_2 \rightarrow HO_2 \tag{R-8}$$

$$HCO + O_2 \rightarrow CO + HO_2 \tag{R-9}$$

$$H_2O_2 + hv \rightarrow 2OH \quad (\lambda{<}362 \text{ nm}) \tag{R-10}$$

Besides, other oxidants can also be of importance on a regional scale. For example, the NO_3 radical could be a major oxidant in forests (vegetation shadows slow down its photolysis) or in the nocturnal boundary layer at high O_3 regions (Brown and Stutz, 2012). Formed by the reaction of $NO_2 + O_3$ (R-11), high NO_3 levels usually occur at night, concerning its very rapid photolysis during the daytime (R-12) and (R-13). Moreover, high NO_3 concentrations are only observed for high O_3 and medium NO_x concentrations in the absence of significant levels of NO caused by reaction (R-15). Like OH, NO_3 also has high reactivity with various trace gases (Brown and Stutz, 2012; Mellouki et al., 2021). For example, NO_3 reacts with NO_2 to form N_2O_5 (R-14), which can undergo hydrolysis on wet surfaces or clouds to produce HNO_3 (or NO_3^-) (R-16) or decomposition back to $NO_3 + NO_2$ (R-17). NO_3 can also react with various organic compounds to form secondary organic aerosol (SOA). For instance, NO_3 reacts with isoprene (C_5H_8), leading to significant organic nitrates (e.g., alkyl nitrates) production (Rollins et al., 2009).

$$NO_2 + O_3 \rightarrow NO_3 + O_2 \tag{R-11}$$

$$NO_3 + hv \rightarrow NO + O_2 \quad (\lambda{<}690 \text{ nm}) \tag{R-12}$$

$$NO_3 + hv \rightarrow NO_2 + O \quad (\lambda{<}690 \text{ nm}) \tag{R-13}$$

$$NO_2 + NO_3 \rightarrow N_2O_5 \qquad \text{(R-14)}$$

$$NO + NO_3 \rightarrow 2NO_2 \qquad \text{(R-15)}$$

$$N_2O_5 + H_2O \xrightarrow{surface} 2HNO_3 \ (or \ 2NO_3^-) \qquad \text{(R-16)}$$

$$N_2O_5 \rightarrow NO_2 + NO_3 \qquad \text{(R-17)}$$

In the past decade, particle pollution, such as $PM_{2.5}$, is going down while O_3 pollution is increasing in many cities of China (Han et al., 2020; Li et al., 2019; Sun et al., 2016, 2019). Especially in the North China Plain (NCP), air pollution becomes a major environmental risk for the public health of >330 million people living in this region. This raises efforts in exploring the NO_x-VOCs-O_3 chemistry. Meanwhile, high O_3 indicates an enhanced atmospheric oxidizing capacity; that is, elevated OH and NO_3 levels are expected. However, very few observations have been reported of OH and NO_3 levels, as well as their production (e.g., HONO photolysis or $NO_2 + O_3$) or loss (e.g., to oxidize primary pollutants), have been reported in the high-O_3 region of the NCP by far (Lu et al., 2019; Suhail et al., 2019). Herein, we provide the first HONO measurements at the foot of Mt. Tai (in Tai'an city, a typical urban site), followed by measurements at the summit of Mt. Tai in the summer of 2018. Data from the summit station is presented in the companion paper, in which daytime HONO formation and its role in the atmospheric oxidizing capacity at the summit level are studied. In this paper, coupled with the box model, the HONO budget and the radical chemistry at the ground level are explored and discussed.

2 Methods

2.1 Field Campaign

2.1.1 Measurement Sites

In the summer (from late May to July) of 2018, a comprehensive field campaign was conducted to understand the atmospheric oxidizing capacity and O_3 pollution in Tai'an, a city in the middle of the NCP. Tai'an is located nearly in the middle between Beijing and Shanghai. The city has a population of about 5.6 million and is about 60 km south of Jinan city (the capital city of Shandong province, population: ~8.7 million). Measurements were conducted both at the ground level (the foot of Mt. Tai, 150 m a.s.l.) and the summit level (the summit of Mt. Tai, 1534 m a.s.l., 36.23°N, 117.11°E). The foot station was inside Shandong College of Electric Power (36.18°N, 117.11°E) in the Taishan district of Tai'an city. There are no industrial activities around this site, which is surrounded by the campus, residential area, and a business district. The 801st province road is in the northeast of this typical urban site. Inside the campus (about 50 ha) frequent traffic was not observed, but it sometimes occurred on the urban roads nearby. Mt. Tai is located in the north part of Tai'an city. Locations of these two stations on the map can be found in the companion ACP paper (entitled "Atmospheric Measurements at Mt. Tai - Part I: HONO Formation and Its Role in the Oxidizing Capacity of the Upper Boundary Layer", Xue et al. (2021a)).

Measurements at these two stations allow us to study HONO formation and its role in the atmospheric oxidizing capacity of the lower (the foot study) and the upper boundary layer (the summit study). Briefly, in the summit study, we found remarkably high daytime HONO levels as well as high unknown HONO source strength, which was mainly caused by rapid vertical transport from the ground to the summit levels driven by mountain winds.2.1.2 Instrumentation

HONO mixing ratios were continuously measured by the LOPAP technique (LOPAP-03, QUMA GmbH, Germany) (Heland et al., 2001; Kleffmann et al., 2006) from 29th May to 8th July 2018 at the foot station, followed by measurements at the summit station from 9th to 31st July 2017. At the foot station, NO-NO_2-NO_x, O_3, CO, and SO_2 were online measured by a series of Thermo Fisher Scientific instruments (42i, 49i, 48i, and 43i, respectively). Because chemiluminescence techniques using molybdenum converters were reported to overestimate the NO_2 level caused by interferences of other NO_y species, the measured NO_2 was corrected with a family constraint in a model run (see Section 3.1.2). VOCs (56 species) and OVOCs (15 species) were measured by a homemade GC-FID instrument (Liu et al., 2016) and the USEPA DNPH-HPLC method (Wang et al., 2020), respectively. Gas-phase H_2O_2 was measured by a monitor based on the wet chemical method (AL2021, Aerolaser GmbH, Germany), details of which can be found in Ye et al. (2018). Water-soluble inorganic particle species (i.e., NO_3^-, SO_4^{2-}, Cl^-, Na^+, K^+, Ca^{2+}, etc.) of $PM_{2.5}$ were collected on Teflon filters every two hours at a sampling flow of 100 L min^{-1} and analyzed by an ion chromatograph (Liu et al., 2020).

Meteorological parameters, including atmospheric temperature (T), pressure (p), relative humidity (RH), wind direction (WD), wind speed (WS), and solar irradiance (Ra) were continuously measured by an auto meteorological station. $J(NO_2)$ was measured by a 4-π filter radiometer (Metcon GmbH, Germany). 10-min average data (except for $PM_{2.5}$) were used for the analysis of time series and statistic descriptions of the data. In contrast, hourly data were used for model simulations. $PM_{2.5}$ measurements were obtained from the Tai'an monitoring station (200 m east of the foot station), and only hourly average data were available. Other J-values used in this study, including $J(HONO)$, $J(O(^1D))$, $J(H_2O_2)$, $J(HCHO)_{rad}$, and $J(HNO_3)$, are calculated by the box model based on trigonometric SZA functions (MCM default photolysis frequency calculation, see Jenkin et al. (1997)) and scaled by the measured $J(NO_2)$. For instance, $J(HONO) = J(HONO)_{model}*J(NO_2)_{measured}/J(NO_2)_{model}$.

2.2 Model Description

2.2.1 Box Model and Constraints

The **F**ramework for **0**-**D** **A**tmospheric **M**odeling, F0AM v4.0 (available at https://github.com/AirChem/F0AM) developed by Wolfe et al. (2016) was used to explore the HONO budget and the radical chemistry. The MCM v3.3.1 chemical mechanism was obtained from http://mcm.leeds.ac.uk/MCMv3.3.1/home.htt. Note that the present F0AM model could also be run with family constraints (see details in Wolfe et al. (2016)), such as the NO_y and Cl_y families, etc. Hence, it allows us to correct for interferences in the NO_2 measurements by the chemiluminescence method (see Section 3.1.2).

The model was constrained by the measured $J(NO_2)$, T, RH, P, VOCs, OVOCs, and all the other measured inorganic species, including the corrected NO_2 by the family constraint. Continuous VOCs measurements were available from 12th June to 6th

July, and hence box model simulations were performed during this period. While J(NO$_2$) measurement was available from 16th June, J(NO$_2$) from 12th to 16th June was estimated through the high quadratic correlation (R^2 = 0.96, Figure S1) between J(NO$_2$) and solar irradiance.

2.2.2 Model Scenarios

155 Table 1 shows the description of different model scenarios. A base case (Sce-0) with all the measured parameters as constraints was run to simulate radical concentrations and their production/loss rates. The family constraint was used in this scenario to correct for interferences of NO$_2$ measurements (Section 3.1.2). Meanwhile, the role of HONO in radical chemistry was also explored by several model sensitivity tests with reducing or increasing the constrained HONO.

With the simulated OH and the corrected NO$_2$ from the base case, we could further explore the HONO budget. Three model
160 scenarios were conducted to assess the potential contributions of different HONO sources, including one with only the default model source (Sce-1), and one with all the six additional sources, including direct emission, dark and photo-enhanced NO$_2$ uptake on aerosol and ground surfaces and nitrate photolysis (Sce-2). In Sce-3, photo-enhanced NO$_2$ uptake on the ground surface was reduced by a factor of 10, aerosol-derived sources (NO$_2$ uptake on the aerosol surface or particulate nitrate photolysis) were significantly enhanced (see Section 3.2.3) to test whether the aerosol-derived sources could well explain the
165 observations.

Table 1: Description of different model scenarios.

Scenarios	Constraints	Objectives
Sce-0	All measurements; NO$_z$ family constraint	NO$_2$ correction; radical concentration and chemistry
Sce-1	All measurements + corrected NO$_2$ and simulated radicals from Sce-0	HONO simulation with NO+OH
Sce-2	Same as Sce-1	HONO simulation with additional sources
Sce-3	Same as Sce-1, but with reduced ground NO$_2$ uptake and enhanced aerosol-derived sources	Testing the performance of aerosol-derived sources

3. Results and Discussion

3.1 Overview of the Measurements and Potential Interferences

3.1.1 Overview of the Measurements

170 Figure 1 shows the meteorological parameters measured at the foot station. During the campaign, it was generally sunny except slightly rainy (<10 mm) on 9th, 10th, 13th, and 28th and heavy rainy (~100 mm) at night of 25th/26th June. Ambient temperature

was normally around 25 ℃ at night and around 30 ℃ during the daytime, except for rainy days when the temperature was relatively low. The relative humidity (RH) was high (up to 80%) on those rainy or cloudy days and low (around 40%) on other days. Campaign-averaged temperature and RH were 27.5 ℃ and 46.6%, respectively (Table 2). Air masses observed at this site originated from multiple directions, including west, south, and east, which are shown in the wind rose plot in Figure S2A. Wind speed was generally low, with an average of about 2 m s^{-1}. In addition, the wind rose results generally agree well with HYSPLIT trajectory results in Figures S2B and S2C.
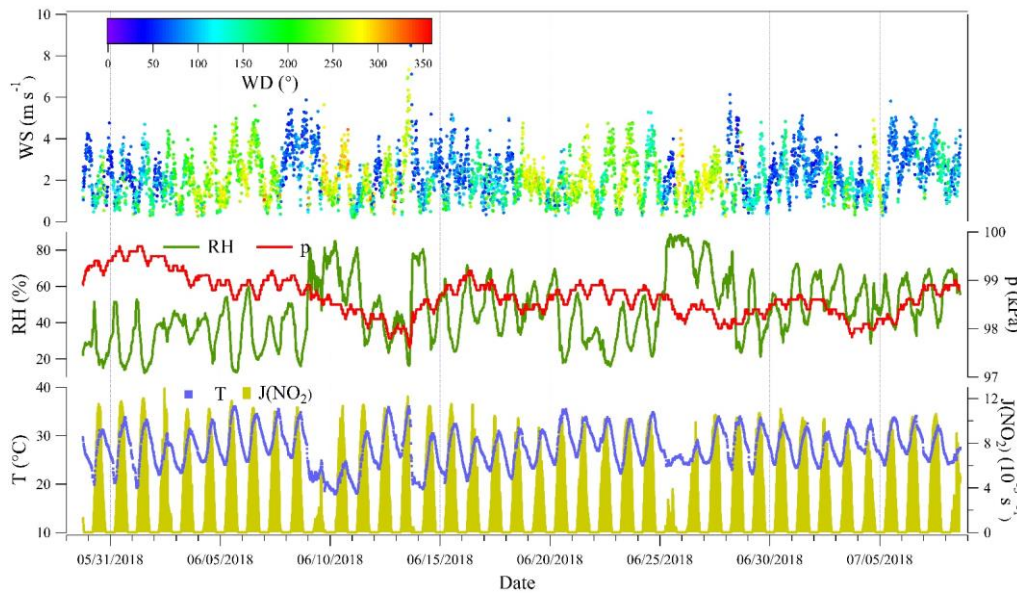
Figure 1: Meteorological parameters measured at the foot of Mt. Tai during the campaign.

Table 2: Statistic summary of meteorological parameters and the measured species. Note that the observation data point number (Obs) of hourly PM$_{2.5}$ is about 1/6 of others (10 min time resolution). The measured rather than the corrected NO$_2$ was used here. SD: standard deviation; Min: minimum; Max: maximum.

Parameters	Mean	SD	Median	Min	Max	Obs
WS (m s^{-1})	2.2	1.1	2.1	0.2	9.7	5749
RH (%)	46.6	17.5	44.9	12.2	88.7	5749
P (kPa)	98.7	0.4	98.6	97.6	99.7	5749
T (℃)	27.5	3.8	27.4	17.9	36.1	5749
J(NO$_2$) (s^{-1})	3.2E-03	3.7E-03	1.0E-03	0	1.1E-02	3183
O$_3$ (ppbv)	63	31	62	0.1	145	5727
PM$_{2.5}$ (μg m^{-3})	29	12	28	10	66	959
CO (ppmv)	0.28	0.25	0.20	0.01	2.08	5717
SO$_2$ (ppbv)	3.6	4.0	2.2	0	36.2	5648
NO (ppbv)	2.0	8.3	0.3	0	126.0	5749
NO$_2$ (ppbv)	15.2	10.8	12.3	0	78.8	5601
HONO (ppbv)	0.62	0.42	0.52	0.05	2.97	5423

In Figure 2 and Figure S3 the measured HONO and related species at the foot station and their diurnal variation profiles are presented, respectively. The measured HONO showed a typical diurnal variation with accumulation after sunset and decay

185 after sunrise. Mixing ratios of the measured HONO varied from 0.05 to about 3 ppbv, with an average of 0.62 ± 0.42 ppbv. The measured NO_2 showed a very similar variation to HONO, and their correlation was high (R = 0.73), indicating a potential role of NO_2 in HONO formation. Severe O_3 pollution (maximum: 145 ppbv) was observed at this site, with O_3 levels frequently exceeding the Class-1 limit value (1-h 160 µg m^{-3}, equivalent to 82 ppbv at 298 K and 101 kPa) of the National Ambient Air Quality Standard of China (GB3095-2012), while the NO_x level was typically lower than O_3. Consequently, a relatively low

190 NO was frequently found, whose concentration was generally lower than 1 ppbv, except for some fresh plumes with higher NO concentrations inside. The two primary pollutants, CO and SO_2, were generally lower than 0.5 ppmv and 5 ppbv, respectively, except for several polluted events, within which CO and SO_2 reached around 2 ppmv and around 35 ppbv, respectively. However, all the primary pollutants, including NO, CO, and SO_2, showed poor correlations with HONO (R = 0.49, 0.44, and 0.13, respectively), implying the minor role of direct emission in HONO formation. The measured hourly $PM_{2.5}$

195 varied from 10 to 66 µg m^{-3}, with an average of 29 µg m^{-3}. The correlation of $PM_{2.5}$ and HONO was very low (R = 0.06), suggesting a minor role of aerosol-derived sources in HONO formation. More discussion on the HONO budget is presented in Section 3.2.
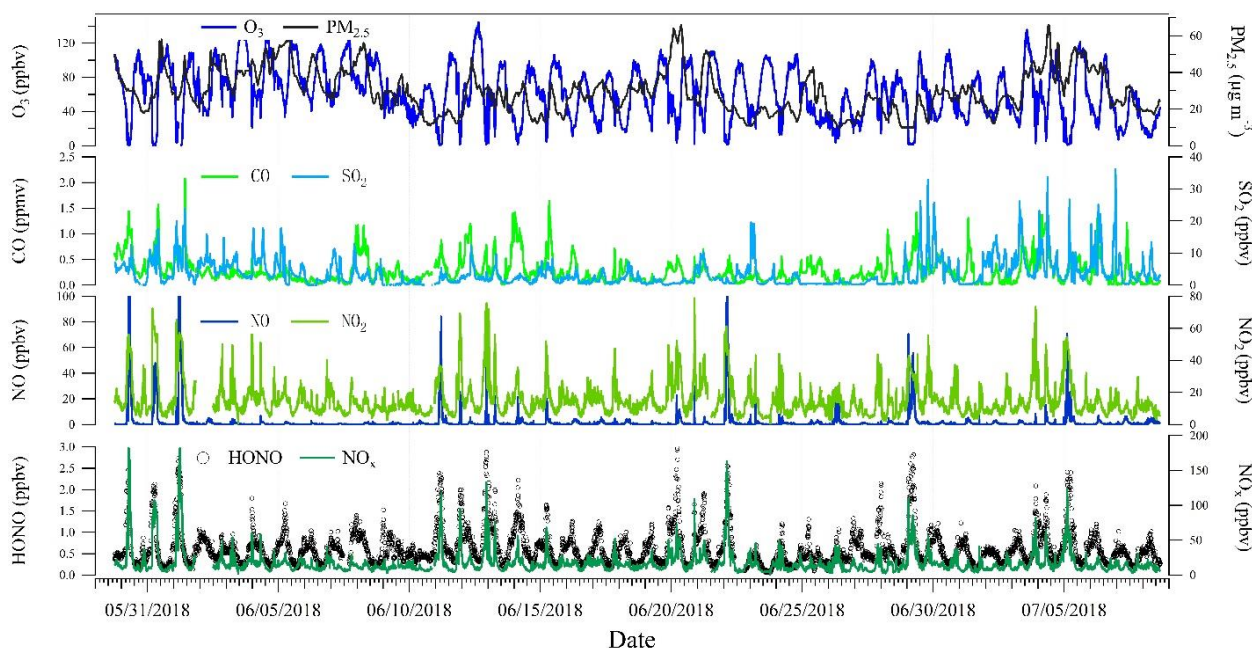
Figure 2: HONO and related species measured during the campaign.

200 Compared to other summertime measurements worldwide (Table 3), the measured HONO level at this site is similar to some measurements in China, such as Beijing in 2007 (Hendrick et al., 2014), Beijing in 2008 and 2017 (Crilley et al., 2019; Hendrick et al., 2014) and Guangzhou in 2006 (Yang et al., 2014); in Europe, such as Milan in 1998 (Alicke et al., 2002) and

Rome in 2001 (Acker et al., 2006); and in North America, such as New York in 2001 (Ren et al., 2003) and Colorado in 2011 (Vandenboer et al., 2013). Besides, it is lower than measurements in cities during polluted periods, such as Jinan in 2016 (Li
205 et al., 2018), Santiago de Chile in 2005 (Elshorbany et al., 2009), Santiago de Chile in 2009 (Villena et al., 2011), and Mexico in 2003 (Volkamer et al., 2010), but higher than recent measurements near European cities, including Forschungszentrum Karlsruhe (Kleffmann et al., 2003), Forschungszentrum Jülich (Elshorbany et al., 2012), suburban Paris (Michoud et al., 2014), and Cyprus (Meusel et al., 2016). It is noteworthy that the measured HONO at the foot station is significantly higher than that observed at the summit station in the same summer, indicating possibly different roles and formation paths of HONO at these
210 two stations.

Table 3: Examples of worldwide HONO measurements at the ground level.

Location	Period	Techniques	Mean (pptv)	Range (pptv)	HONO/NO$_x$ %	Reference
Europe						
Milan	May-Jun 1998	DOAS	920[a]/140[b]	<4400		(Alicke et al., 2002)
Pabstthum	Jul-Aug 1998	DOAS	330[a]/70[b]	<1200	1.4[a]/1.0[b]	(Alicke et al., 2003)
Rome	May-Jun 2001	LP-DOAS, DNPH-HPLC, WEDD	580	<2000	3[*]	(Acker et al., 2006)
Forschungszentrum Karlsruhe	Oct 2001	LOPAP	400	180-1100	1-6[a]	(Kleffmann et al., 2003)
Forschungszentrum Jülich	Jun-Jul 2005	LOPAP	220	50-1100	2 (0.6-12)	(Elshorbany et al., 2012)
Suburban Paris	Jul 2009	Ni-troMAC	~150	10-500		(Michoud et al., 2014)
Cyprus	Jul-Aug 2014	LOPAP	35	<300	33	(Meusel et al., 2016)
South America						
Santiago de Chile	Mar 2005	LOPAP	2500[a]/2300[b]	670-7100	3.9 (1.3-9.2)	(Elshorbany et al., 2009)
Santiago de Chile	Nov 2009	LOPAP	1500/1100[**]	220-3800/150-4600[**]	2.0 (0.7-5.9)	(Villena et al., 2011)
North America						
California	Aug-Sep 1979	DOAS	1090[a*]/<280[b]	<4100		(Platt et al., 1980)
New York	Jul-Aug 2001	HPLC	660	400-1400		(Ren et al., 2003)
Colorado	Feb-Mar 2011	NI-PT-CIMS	500[a*]/100[b]	<2000	3.5-7.6[a]	(Vandenboer et al., 2013)
Mexico	Mar-May 2003	LP-DOAS	1200[*]	<3000		(Volkamer et al., 2010)
China						
Beijing	Aug-Sep 2004	DOAS		<6100	8.4[c]	(Qin et al., 2006)
Guangzhou	Jun 2006	LOPAP	950[a]/240[b]	10-5000	4.3[a]/4.5[b]	(Li et al., 2012)
Yufa	Jul-Aug 2006	LOPAP	890[a] /430[b]	30-3600	4.6[a]/4.8[b]	(Yang et al., 2014)
Beijing	Aug 2007	DOAS	1450	440-2900	5[c]	(Spataro et al., 2013)
Beijing	Jul 2008	DOAS	180[d]	100-800	0.8[cd]	(Hendrick et al., 2014)
Xianghe	Jun 2012	DOAS	90[d]	100-700	1.7[cd]	(Hendrick et al., 2014)
Jinan	Jun-Aug 2016	LOPAP	1200[a]/1010[b]	<6000	6[a]/5[b]	(Li et al., 2018)
Wangdu	Aug 2016	SCIC	230	30-1140	2.1[b]	(Xue et al., 2021c)
Wangdu	Jun 2017	LOPAP	360[e]/720[f]/1360[g]	260-860[e]/320-1490[f]/400-3130[g]	2.6[e]/5.4[f]/11.8[g]	(Xue et al., 2021c)
Beijing	May-Jun 2017	Intercomp.[h]		~100-10000		(Crilley et al., 2019)
Tai'an	May-Jul 2018	LOPAP	620	50-2970	4.2	This study
Mt. Tai Summit	Jul 2018	LOPAP	133	1880	6.4	This study

[a]: night-time, [b]: daytime, [c]: HONO/NO$_2$, [d]: noontime, [e]: non-fertilization period, [f]: pre-fertilization period, [g]: intensive fertilization period, Intercomp[h]: intercomparison of 5 instruments.

*: half of the diurnal maximum.

215   **: 3rd and 21st floors, respectively.

3.1.2 NO$_2$ Interference and Correction

As the most important HONO precursor, accurate measurement of NO$_2$ plays a key role in analyzing HONO formation. The NO$_x$ monitor used in this study could specifically detect NO. To measure NO$_2$, a molybdenum converter is used to convert NO$_2$ to NO. However, this chemical conversion process suffers from the interference of other NO$_y$ species (Villena et al.,

220   2012), primarily including inorganic species such as (measured) HONO, (non-measured) HNO$_3$, HNO$_4$, N$_2$O$_5$, and NO$_3$, peroxyacyl nitrates (PANs, RC(O)OONO$_2$), organic nitrates (RONO$_2$), and peroxy nitrates (ROONO$_2$), etc. In this study, we defined the sum of RONO$_2$ and ROONO$_2$ as organic nitrates*. Hence, the measured NO$_2$ is the sum of real NO$_2$ and those interfering species. HONO was measured and subtracted from the measured NO$_2$, and we defined NO$_2$* = the measured NO$_2$ – HONO. As NO$_2$ is the most important HONO precursor, we used the family constraint (NO$_2$* = NO$_2$ + HNO$_4$ + 2N$_2$O$_5$ +

225   NO$_3$ + PANs + organic nitrates*) in the base case (Sce-0) to separate each species from NO$_2$*. To describe the PANs class, PAN, PPN, and MPAN (MCM names, see their structures at http://mcm.leeds.ac.uk/MCMv3.3.1/) were considered. In the organic nitrates* class, CH3NO3, C2H5NO3, NC3H7NO3, IC3H7NO3, TC4H9NO3, NOA, ISOP34NO3, ISOPANO3, ISOPDNO3, ISOPCNO3, and ISOPBNO3 (MCM names) were included. Considering that HNO$_3$ is very sticky, we expect HNO$_3$ was mostly absorbed by the filter and/or sampling tubes before the converter rather than being converted to NO by the

230   converter. Therefore, HNO$_3$ was generally not included in the family constraint and only considered for the uncertainty analysis. Figure 3 shows the model results of the relative contribution of each NO$_2$* species to NO$_2$*. At night with the absence of photochemistry, the real NO$_2$ dominated NO$_2$* components, with a contribution of >95%, suggesting a small interference on the NO$_2$ measurement. However, the contribution of real NO$_2$ was found to decrease during the daytime due to the increasing interference. For example, at 11:00, the real NO$_2$ contributed 82% of the NO$_2$*, indicating that the interferences could be as

235   high as +22% (calculated from 18%/82%). In particular, at 13:00, PANs alone caused the highest interference by +21% (calculated from 17%/81%).

The variations of the simulated PANs and NO$_3$ and their ratios to NO$_2$ were similar to previous observations (Brown and Stutz, 2012; Roberts et al., 1998; Su et al., 2008; Villena et al., 2012; Xue et al., 2011), indicating that the uncertainty of the method is small. For the following model simulations and analysis, only the corrected NO$_2$ was used. Besides, Figure S4 exhibits the

240   parallel test results, in which HNO$_3$ was included in the family constraint. It can be found that the interference became more significant; for instance, the interference could be as high as +75% (calculated from 43%/57%, at 11:00). This represents the upper limit of the interferences, if the sampling tubes and the inlet filter are heated so that HNO$_3$ could have reached the converter.
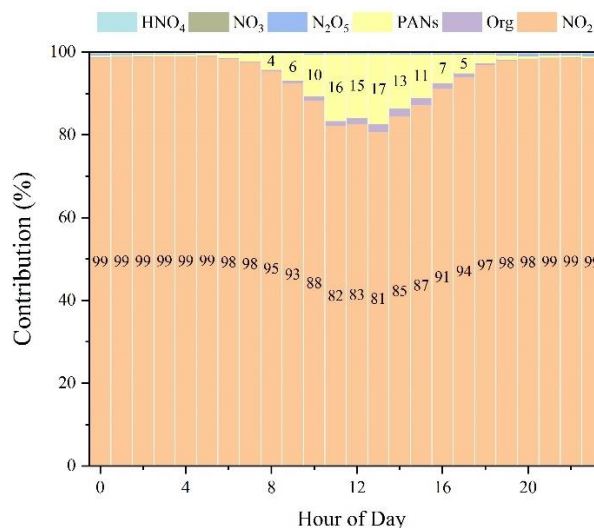
Figure 3: Relative contribution of each NO_2^* species. PANs = PAN + PPN + MPAN. Org represents organic nitrates[*] ($RONO_2$ + $ROONO_2$).

Additionally, as shown in Figure S5, the simulated HNO_4 showed 1) a different diurnal variation from, 2) generally $1 - 2$ orders of magnitude lower concentrations than, and 3) a very poor correlation ($R^2 = 0.06$) with the observed HONO, indicating its negligible interference on the HONO measurement by the LOPAP technique (Legrand et al., 2014). It is worth noting that for the description of O_3 formation in the polluted atmosphere, accurate measurements of d NO_x and HONO are necessary.

3.2 HONO Sources and Budget

3.2.1 Model Default Source (NO + OH) and Unknown Source Strength

The homogeneous reaction of NO and OH has been adopted as the default HONO source in atmospheric chemistry models, including MCM. Model results from Sce-1 that only contains the homogeneous source with the modeled OH from Sce-0 are shown in Figure 4. Apparently, the source of NO + OH is too small to explain the observed HONO as the simulated one is almost one order of magnitude lower than observations. Its contributions to the measured daytime and night-time HONO are 15% and 12%, respectively.
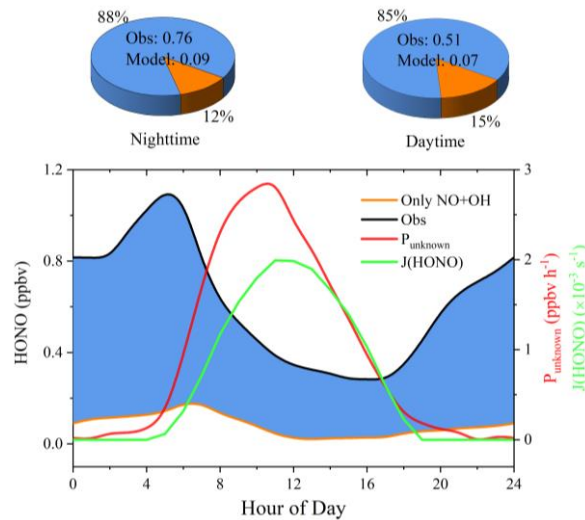
Figure 4: Simulated HONO by the default mechanism (Sce-1, left axis) compared with the observations (Obs, left axis), unknown source strength ($P_{unknown}$, right axis), HONO photolysis frequency (J(HONO), right axis). The relative contributions of NO + OH to the observations at night (19:00 – 4:50) and day (5:00 – 18:50) were shown in the left and the right pie charts, respectively. The shaded area in blue represents the difference between the observation and modeled values.

Then we calculated the unknown source strength ($P_{unknown}$) based on the following equation (Sörgel et al., 2011; Su et al., 2008).

$$P_{unknown} = \frac{\Delta HONO}{\Delta t} + L(HONO)_{pho} + L(HONO)_{HONO+OH} - P(HONO)_{NO+OH} \qquad \text{(Eq-1)}$$

265 The HONO loss rates through photolysis ($L(HONO)_{pho}$) and reaction with OH ($L(HONO)_{HONO+OH}$) and production rate from NO + OH were obtained from the base model scenario (Sce-0 with a constraint of the measured HONO). HONO mixing ratio differences within a one-hour interval, $\frac{\Delta HONO}{\Delta t}$, were calculated by the measurement, and are compared with $P_{unknown}$ in Figure S6. As shown in Figure 4, $P_{unknown}$ rapidly increased in the morning and peaked at nearly 3 ppbv h^{-1} at 11:00, followed by a decrease, revealing a photo-enhanced source. Note that the profile of $P_{unknown}$ was asymmetric around 11:00, indicating the

270 unknown source is not simply photolytic but also includes its precursors that also have an asymmetric distribution (e.g., NO_2, Figure S3). The possible additional HONO sources that are responsible for $P_{unknown}$ are discussed in the following section.

3.2.2 Additional Sources vs. $P_{unknown}$

3.2.2.1 Direct Emission: ΔHONO/ΔNO$_x$ Ratio

The ΔHONO/ΔNO$_x$ ratio for the direct emission was determined from fresh plumes, which reached the following requirements:
275 1) at night when photolysis was absent, 2) rapid NO increase by >10 ppbv within 10 min. Only 17 cases were obtained throughout the campaign due to the persistent high O_3 and the fast NO-to-NO$_2$ conversion. If NO is completely titrated by O_3, there is a risk that the plume may not be fresh and that the inferred ΔHONO/ΔNO$_x$ might be overestimated due to heterogeneous secondary HONO sources. In Table 4 the obtained ΔHONO/ΔNO$_x$ was shown, varying from 0.18% to 1.86%, with an average of 0.98% and a median of 0.90%. The inferred value might be larger than the real one as potential NO$_2$-to-

HONO conversion leads to an overestimation. This is consistent with the observation that the inferred $\Delta HONO/\Delta NO_x$ is generally higher in high RH conditions due to the potential NO_2-to-HONO conversion (Figure 5). More importantly, we found that the observed $HONO/NO_x$ is convergent as NO/NO_2 increases (Figure 5), which allows a further correction of $\Delta HONO/\Delta NO_x$. The reported NO/NO_2 ratios from combustion processes show significant variations, e.g., 6.7 in Wuppertal (Kurtenbach et al., 2012), ~18 in Denver (Wild et al., 2017), 5 – 30 in London (Carslaw and Beevers, 2005), and 13 – 43 from China IV/V vehicles (He et al., 2020). Furthermore, in the emission inventory, the NO/NO_2 emission ratio in the NCP is about 9 (Zhang et al., 2009). However, the measured night-time NO/NO_2 ratios were less than 3 (Figure 5), much lower compared to direct emission measurements, indicating that the observed plumes were not fresh enough to directly obtain the primary $\Delta HONO/\Delta NO_x$ emission ratio. By using a typical NO/NO_2 ratio of 10 from car exhaust, the calculated $\Delta HONO/\Delta NO_x$ through the convergent function (Figure 5) is 0.7%, similar to that obtained from laboratory or tunnel experiments (Kirchstetter et al., 1996; Kramer et al., 2020; Kurtenbach et al., 2001; Liu et al., 2017a).

Caused by its fast daytime photolysis, direct HONO emissions (HONO$_{emi}$) are likely significantly overestimated when a constant $\Delta HONO/\Delta NO_x$ ratio is considered, as done in former studies (Kramer et al., 2020; Liu et al., 2017b). Due to the much shorter lifetime of HONO ($\tau(HONO)$) compared to NO_x ($\tau(NO_x)$), a much smaller fraction of the emitted HONO compared to NO_x will survive in the daytime atmosphere. Accordingly, for the first time, we calculated $\tau(HONO)$ and $\tau(NO_x)$ and considered them in the parameterization of HONO$_{emi}$ (see the method in Section 1 of the Supporting Information). As shown in Figure S7A, daytime $\tau(NO_x)$ was typically one order of magnitude higher than $\tau(HONO)$ (Figure S7A), indicating a remarkable overestimation of the contribution of HONO$_{emi}$ to the measured HONO when using a constant $\Delta HONO/\Delta NO_x$ emission ratio (Figure S7B). Hence, HONO$_{emi}$ was quantified by the following equations:

$$\boldsymbol{HONO_{emi} = 0.7\% \times [NO_x]} \text{ (night-time)} \tag{Eq-2}$$

$$\boldsymbol{HONO_{emi} = 0.7\% \times [NO_x] \times \frac{\tau(HONO)}{\tau(NO_x)}} \text{ (daytime)} \tag{Eq-3}$$

In summary, direct emission contributed about 1 – 26% of the measured HONO, with an average of 13%. Moreover, the new method developed here may still have some uncertainties but largely reduces the significant overestimation of the contribution of HONO$_{emi}$ to the observations during daytime compared to using a constant $\Delta HONO/\Delta NO_x$ (Figure S7B).

Table 4: $\Delta HONO/\Delta NO_x$ ratios determined from night-time (19:00 – 4:50) data of the campaign. Concentrations (ppbv) of HONO/NO/NO$_x$ at the start and the end of each plume of fresh emissions are also shown.

Date	Period	HONO		NO		NO$_x$		$\Delta HONO/\Delta NO_x$
1st June	2:20-2:30	1.58	1.77	3.1	13.5	64.4	75.8	1.67%
	4:20-4:30	2.67	2.74	0.6	38.2	36.0	74.2	0.18%
11th June	3:00-3:10	1.32	1.71	0.2	18.9	24.9	50.0	1.55%
	3:50-4:20	1.68	2.21	15.7	71.7	51.3	107.0	0.95%
	4:30-4:40	1.91	2.31	41.2	72.4	75.3	107.3	1.25%
	22:00-22:10	1.41	1.69	1.0	16.6	41.1	78.4	0.75%
	23:30-23:40	1.74	1.99	1.7	17.0	53.2	71.1	1.40%
12th June	22:10-22:30	2.64	2.78	0.8	59.0	68.7	132.9	0.22%

14th June	3:00-3:10	1.43	1.76	6.6	21.2	38.8	56.5	1.86%
20th June	20:50-21:10	0.94	1.65	0.9	29.7	30.0	108.5	0.90%
22nd June	2:10-2:20	1.29	1.98	4.6	95.1	51.8	147.2	0.72%
	2:40-3:00	1.58	2.20	38.3	120.1	83.1	163.7	0.77%
29th June	1:00-1:20	0.96	2.26	3.1	70.5	24.3	109.4	1.53%
	2:20-2:40	0.34	0.40	7.0	21.1	45.6	59.6	0.43%
	4:20-4:30	1.79	1.97	11.7	42.2	44.0	74.0	0.60%
5th July	1:10-1:30	0.77	1.38	0.1	18.2	33.8	70.6	1.66%
	2:10-2:30	1.09	1.26	6.4	71.0	56.2	124.6	0.25%
Mean								0.98%
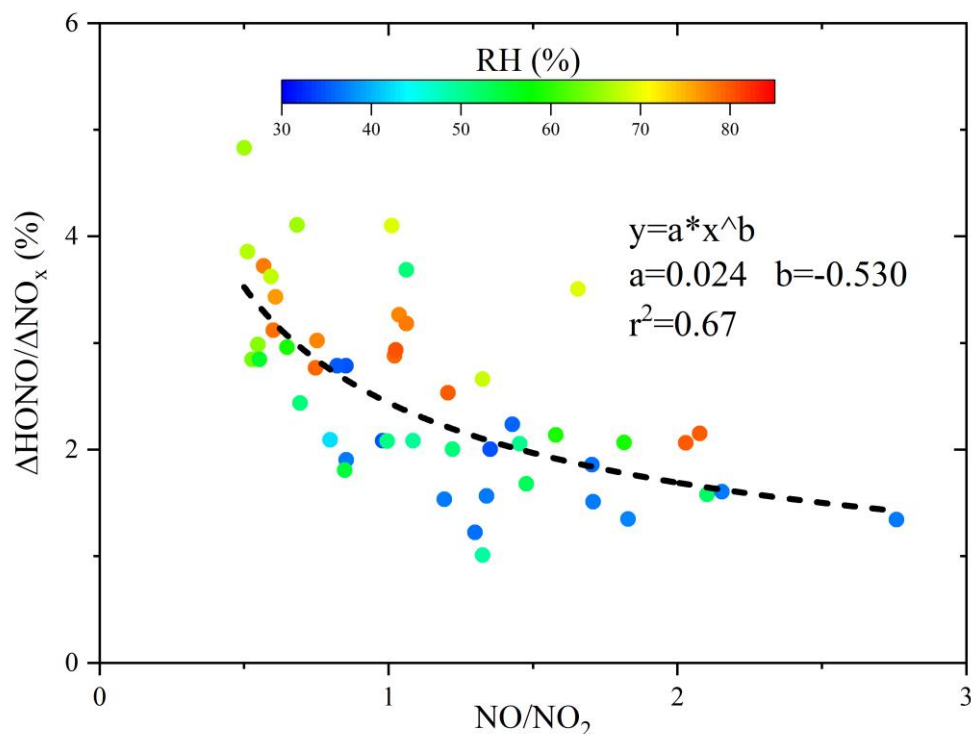
Figure 5: The inferred direct emission ratio ($\Delta HONO/\Delta NO_x$) and NO/NO_2 colored by RH. Only data with $NO/NO_2 > 0.5$ was shown as lower ones indicate much aged rather than fresh plumes.

3.2.2.2 NO₂ Uptake on the Aerosol Surface

Parameterizations of HONO formation from the NO_2 uptake on the aerosol surface without and with photo-enhanced effects ($P(HONO)_{a\_dark}$ and $P(HONO)_a$) are described by (Eq-4) and (Eq-5), respectively. In (Eq-4) and (Eq-5), HONO yields of 50% and 100% were considered for the dark and the photo-enhanced NO_2 conversion, respectively (Finlayson-Pitts et al., 2003; George et al., 2005). A relatively large NO_2 uptake coefficient γ_{a_dark} of 1×10^{-5} was used here to represent its upper limit. Its

overestimation should not cause significant uncertainties as P(HONO)$_{a\_dark}$ was negligible to HONO formation (see the following discussion). For the photo-enhanced NO$_2$ uptake coefficient γ_a values of 1.3×10^{-4} (upper limit derived from the summit measurement, see Xue et al. (2021b)) and 2×10^{-5} (more realistic value derived from laboratory experiments, see Stemmler et al. (2006 and 2007)) were used in (Eq-5) to constrain the upper limit and a more realistic value of P(HONO)$_a$.

$$P(HONO)_{a\_dark} = \frac{v(NO_2)\times S_a \times [NO_2]}{8} \times \gamma_{a\_dark}, \tag{Eq-4}$$

$$P(HONO)_a = \frac{v(NO_2)\times S_a \times [NO_2]}{4} \times [\gamma_a \times \frac{J(NO_2)_{measured}}{0.005\ s^{-1}}], \tag{Eq-5}$$

$\upsilon(NO_2)$, S$_a$, [NO$_2$], and J(NO$_2$)$_{measured}$ denote the average NO$_2$ molecular speed (m s^{-1}), aerosol surface density (m^{-1}), NO$_2$ concentration (ppbv), and the measured NO$_2$ photolysis frequency (s^{-1}), respectively. As aerosol size distribution measurements were not available at the foot station, we estimated S$_a$ based on the measured PM$_{2.5}$ concentrations as they were highly correlated. For instance, measurements at the summit station during this campaign and other sites in the NCP found high correlations between PM$_{2.5}$ and S$_a$ (derived from particle size distribution measurement) with a S$_a$/PM$_{2.5}$ ratio of about 8×10^{-6} – 1.3×10^{-5} m^2 µg^{-1} (Wu et al., 2008; Xue et al., 2020). Here a S$_a$/PM$_{2.5}$ ratio of 1.0×10^{-5} m^2 µg^{-1} was used, and its uncertainty will not cause significant changes in the HONO simulations because of its small contribution (see the following discussion). Diurnal variations of P(HONO)$_{a\_dark}$ and P(HONO)$_a$, in comparison with P$_{unknown}$ and P(HONO)$_{NO+OH}$, are shown in Figure 6A. Clearly, both P(HONO)$_{a\_dark}$ and P(HONO)$_a$ were negligible compared to daytime P$_{unknown}$. P(HONO)$_a$ increased with γ_a, but even when using the upper limit of $\gamma_a = 1.3\times10^{-4}$, it was still too small to be comparable to P(HONO)$_{NO+OH}$ and far from explaining P$_{unknown}$. This observation reveals minor impacts of heterogeneous HONO formation on particle surfaces to the missing HONO source, particularly during daytime.
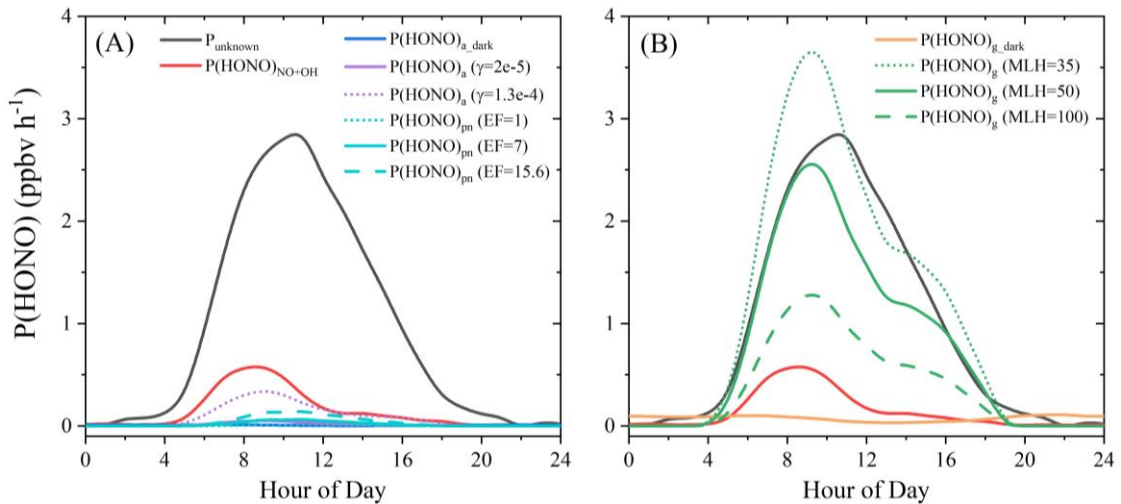
Figure 6: HONO production rates from different ((A): aerosol-derived, (B): ground-derived) sources and unknown HONO source strength.

3.2.2.3 pNO₃ Photolysis

Parameterization of HONO formation from particulate nitrate photolysis (P(HONO)$_{pn}$) is presented in (Eq-6). Recent studies found that EF values were generally lower than 10, for instance, a value of 7 from a recent field study (Romer et al. 2018).In laboratory studies, even lower values of ~1 were observed (Laufs and Kleffmann, 2016; Shi et al., 2021; Wang et al., 2021). Hence an EF value of 7 was used in the P(HONO)$_{pn}$ calculation, and values of 1 and 15.6 were also used to test the sensitivities (the upper limit value was derived from the summit measurement, see Xue et al. (2021a)).

$$P(HONO)_{pn} = pNO_3 * J(HNO_3) * EF, \qquad \text{(Eq-6)}$$

where pNO₃ and J(HNO₃) represent the measured particulate nitrate (with unit converted from µg m^{-3} to ppbv) and the photolysis frequency of gas-phase HNO₃ (s^{-1}), respectively.

Diurnal variations of P(HONO)$_{pn}$ with different EF values are shown in Figure 6A. With EF varying from 1 to 7, P(HONO)$_{pn}$ was 1 – 2 orders of magnitude lower than P$_{unknown}$. Even using a high EF = 15.6, P(HONO)$_{pn}$ was still significantly less than half of P(HONO)$_{NO+OH}$. Therefore, model results constrained by field measurements and recent kinetics suggested that the two aerosol-derived sources (NO₂ conversion and nitrate photolysis) may not have significant impacts on daytime HONO formation, with their contributions significantly lower than half of P(HONO)$_{NO+OH}$.

3.2.2.4 NO₂ Uptake on the Ground Surface

Parameterizations of HONO production from the NO₂ uptake on the ground surface without and with photo-enhanced effects (P(HONO)$_{g\_dark}$ and P(HONO)$_g$) are demonstrated in (Eq-7) and (Eq-8), respectively. NO₂ uptake coefficients of γ_{g_dark} and γ_g were set to 1.6×10^{-6} and 2×10^{-5} (Han et al., 2016; Stemmler et al., 2006, 2007), respectively. The photo-enhancement effect was described by $\frac{J(NO_2)_{measured}}{0.005\ s^{-1}}$ (Vogel et al., 2003; Wong et al., 2013; Xue et al., 2020).

$$P(HONO)_{g\_dark} = \frac{v(NO_2) \times [NO_2]}{8 \times MLH} \times \gamma_{g\_dark}, \qquad \text{(Eq-7)}$$

$$P(HONO)_g = \frac{v(NO_2) \times [NO_2]}{4 \times MLH} \times \gamma_g \times \frac{J(NO_2)_{measured}}{0.005\ s^{-1}}, \qquad \text{(Eq-8)}$$

As shown above, one of the most important parameters for calculating ground HONO formation in a box model is the mixing layer height (MLH) as it is part of the denominators in both (Eq-7) and (Eq-8). MLH for HONO should be significantly lower than the boundary layer height (BLH) due to its formation on the ground level and its short lifetime, which could be confirmed by gradient measurements (Kleffmann et al., 2003; Meng et al., 2020; Vogel et al., 2003; Wang et al., 2019; Wong et al., 2012; Xing et al., 2021; Ye et al., 2018b). For instance, a recent gradient HONO study by the MAX-DOAS technique in southwest China found a steep HONO gradient from 0 to 4 km (Xing et al., 2021). When considering their measurement at 17:00 (UTC+8) as an example, HONO levels rapidly decreased from 4.8 ppbv at the ground level (~4 m above the ground surface) to 1.6, 0.7, 0.3, 0.2, and 0.1 ppbv averaged in the layers of 0 – 100, 100 – 200, 200 – 300, 300 – 400, and 400 – 500 m above the ground level, respectively. In contrast, both NO₂ and aerosol extinction remarkably increased from the ground level to about 200 m and then decreased with altitude (>200 m). These observations indicate that 1) ground-derived sources dominated daytime

HONO formation; 2) the MLH for HONO was much less than 100 m, and 3) significant overestimation, i.e., by a factor of >3 in Xing et al. (2021), could be expected if using measurements on the ground surface to represent the average HONO within an MLH higher than 100 m. A similar phenomenon could also be found in Brown et al. (2013) and Vandenboer et al. (2013). Therefore in the present study, the MLH for HONO was set at a constant height of 50 m, with sensitivity tests performed with the MLH set at 35 and 100 m. Similar values (25 – 100 m) were also used in previous box model studies (Lee et al., 2016; Xue et al., 2020, 2021c). It should be highlighted that a box model as used in the present study is not an ideal tool for studying a ground source when comparing with near-ground surface measurements in the atmosphere. For the future, gradient measurements are recommended, which should be compared with 1-D model simulations.

Diurnal variations of $P(HONO)_{g\_dark}$ and $P(HONO)_g$, in comparison with $P_{unknown}$ and $P(HONO)_{NO+OH}$, are shown in Figure 6B. $P(HONO)_{g\_dark}$ is the largest HONO source during the night-time, while it was negligible during the daytime, which is consistent with many previous studies (Li et al., 2010; Liu et al., 2019; Vogel et al., 2003; Xue et al., 2020; Zhang et al., 2019b, 2019a, 2016). Considering the photo-enhanced formation, $P(HONO)_g$ shows a similar shape and a similar level to daytime $P_{unknown}$, indicating the potential dominance of $P(HONO)_g$ in the daytime HONO formation. When changing MLH to 100 (or 35) m, the level of $P(HONO)_g$ becomes much lower (or higher) than $P_{unknown}$. Due to this, sensitivity tests on MLH were conducted but in Sce-2 a constant MLH of 50 m was used. Small differences in the shapes of measured and modeled results may be also caused by the variable MLH induced by variable vertical mixing in the atmosphere and the variable photolytic lifetime of HONO during the daytime.

3.2.3 HONO Budget

Along with the previous discussion, we conducted a model run (Sce-2) with all the discussed HONO sources. As shown in Figure 7, this model performed well in predicting HONO, indicating reasonable parameterizations of the HONO sources. Here, the time series of the modeled HONO were very consistent with those of the observations both for the variations and the absolute levels. An exception was only the heavy rain period from 25th to 28th June (see the next section). In particular, the model exhibited very high performance in predicting noontime (10:00 – 16:00) HONO as the modeled HONO was very close to the observed HONO (Figure 7B). Moreover, in Sce-3 we reduced γ_g by a factor of 10 and enlarged γ_a from 2×10^{-5} to 1.2×10^{-3} or EF from 7 to 400. While that the modified model could also generally predict the observed HONO levels (Figures S8A and S9A) but it largely failed to reproduce the noontime observations in levels and variations (Figures S8B and S9B) including its asymmetry as mentioned in Section 3.2.1. This observation reinforces our conclusion that aerosol-derived sources play only a minor role in daytime HONO formation.
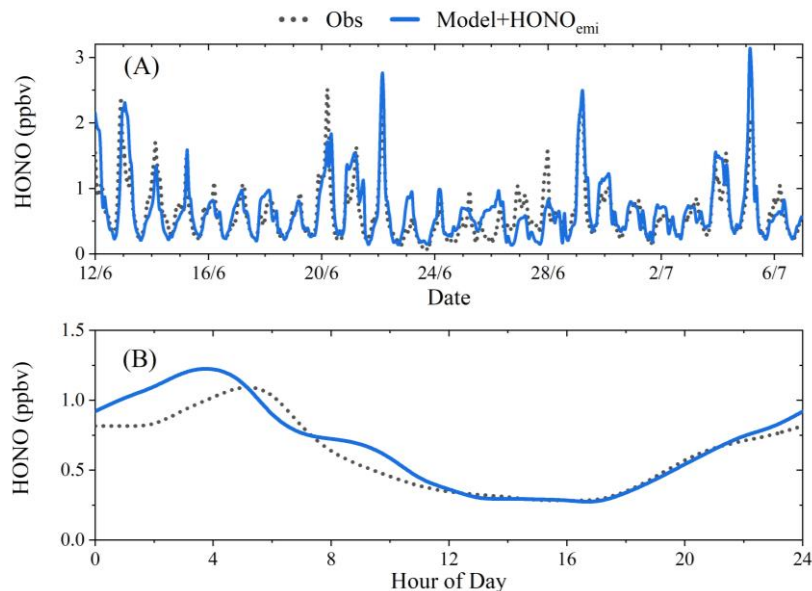
Figure 7: Modeled HONO mixing ratios (Model, in blue) in comparison with observations (Obs, in black). (A): time series; (B): average diurnal variations. Model+HONO_emi represents the sum of the modeled HONO and HONO_emi.

400 Figure 8 displays the diurnal relative contributions of different HONO sources. It clearly shows that dark NO_2 uptake on the ground surface dominated (~70%) night-time HONO formation while photo-enhanced NO_2 uptake on the ground surface dominated (~80%) daytime HONO formation. $P(HONO)_{NO+OH}$ played a moderate role throughout the whole day, with a contribution of 5 – 15% except for a relatively larger contribution (~20%) in the early morning due to high NO levels. Direct emissions made moderate contributions of 15 – 25% at night but negligible ones during daytime. Contributions of

405 $P(HONO)_{a\_dark}$, $P(HONO)_a$, and $P(HONO)_{pn}$ were always lower than 10%, and their contributions could be even smaller when using realistic kinetic parameters derived in recent studies. Therefore, aerosol-derived HONO sources may not significantly contribute to HONO formation for near-ground surface measurements (Chen et al., 2019; Neuman et al., 2016; Sarwar et al., 2008; Vogel et al., 2003; Wong et al., 2013; Xue et al., 2020; Zhang et al., 2016, 2019b).
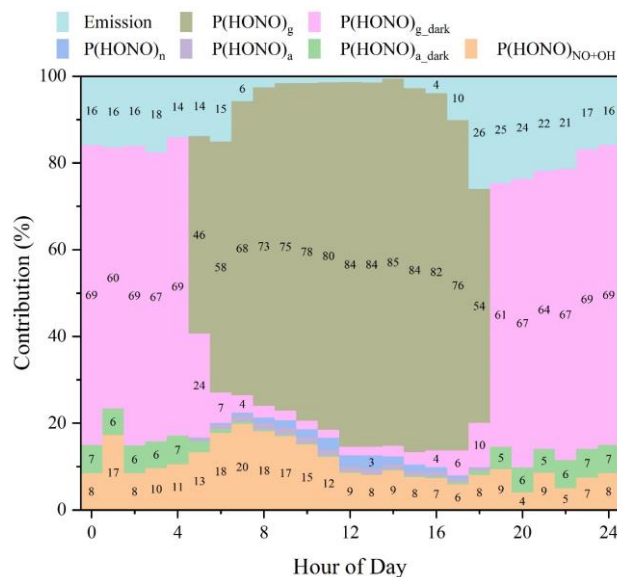
Figure 8: Relative contributions of different HONO sources. Note that the contribution from direct emission was calculated based on the ratio of HONO$_{emi}$ to the observed HONO.

3.2.4 Other Potential Sources

As discussed before, the model (Sce-2) could generally well reproduce most observations except for the period from 25th to 27th June. A significant overestimation occurred from midday of 25th to the morning of 26th, which was caused by the enhanced wet/dry deposition due to the heavy rain (>100 mm, Figure S10) during the night 24th/25th. In contrast, from midday of 26th to the night of 27th/28th, a significant underestimation by the model was obtained. Besides, an elevation of HONO/NO$_x$ was found during this period (Figure S10). This might be caused by 1) the enhanced HONO emission from urban soil or 2) the enhanced NO$_2$ uptake on the ground surface. HONO emissions from soils may occur through biological processes observed in the laboratory experiments or field measurements over the agricultural fields (Oswald et al., 2013; Scharko et al., 2015; Tang et al., 2019; Xue et al., 2019), while evidence for its occurrence on urban soil surfaces after the rain is still not uncertain. At 13:00 on 26th and 27th June, the model predicted lower HONO by almost a factor of 2 – 4 (observation: 0.45 ppbv on both days; model: 0.13 and 0.21 ppbv), which needs an enhancement of at least 2 – 4 in γ_g if using NO$_2$ uptake on the ground surface to explain the underestimation. Current laboratory studies have studied the enhancement effect of atmospheric RH (in the range of 10 – 70%) on the NO$_2$ uptake coefficient on the humic acid surface with enhancement factors of less than 3 (Han et al., 2016; Stemmler et al., 2006, 2007). Campaign averages of the measured NO$_2$ and RH at 13:00 were 7.4 ppbv and 35.5%, respectively. At 13:00 on 26th (27th) June, the measured NO$_2$ of 7.9 (4.3) ppbv was similar to (or lower than) the campaign average, but the RH of 67.6% (53.1%) was significantly higher than the campaign average. But the RH was still in the range (10 – 70%) for which RH showed a small enhancement effect on γ_g (less than 3). Hence, after rain, an enhanced NO$_2$ uptake may be responsible for the underestimation. In addition, soil HONO emission may co-exist, but more evidence for urban regions was needed. However, the impact of highly humid surfaces (e.g., rainwater on the ground surface) on different HONO

sources and sinks was still unclear. Further studies on the impact of rain on urban soil surface processes are necessary, such as field studies of soil HONO emission fluxes and laboratory studies of NO_2 uptake kinetics on relevant surfaces.

3.3 Radical Chemistry

Comprehensive field measurements in comparison to model studies allow studying the role of HONO in the radical chemistry
435 of the atmosphere. HONO is expected to strongly impact OH levels in the lower atmosphere due to strong daytime HONO sources and due to its fast photolysis. In addition, considering high O_3 levels at the present field site, NO_3 chemistry could also be important particularly during night-time, which will also be discussed in this section.

3.3.1 Role of HONO in Radical Concentrations

Figure 9 shows the simulated radical concentrations in different model scenarios, in which their sensitivities to the constrained
440 HONO were tested. It can be obtained that RO_x radicals (OH, HO_2, and RO_2) were significantly affected by the constrained HONO, implying the vital role of HONO in the RO_x budget. For instance, the peak OH concentration in the base case was 0.42 pptv (equivalent to 1.0×10^7 molecules cm^{-3}). It decreased to 0.37 (or 0.32) pptv when HONO was reduced by 50% (or 100%) and increased to 0.46 (or 0.51) pptv when HONO was enlarged by 50% (or 100%). In contrast, modeled NO_3 concentrations showed very small variations whether HONO was reduced or enlarged. NO_3 concentrations are mainly
445 governed by the levels of $O_3 + NO_2$ during night-time, when HONO has no impact on radical levels, due to its missing photolysis. The almost same radical concentrations in the model cases NO + OH and case -100% indicate the minor role of NO + OH in the radical budget as this OH sink is exactly compensated by the OH production through (R-5).
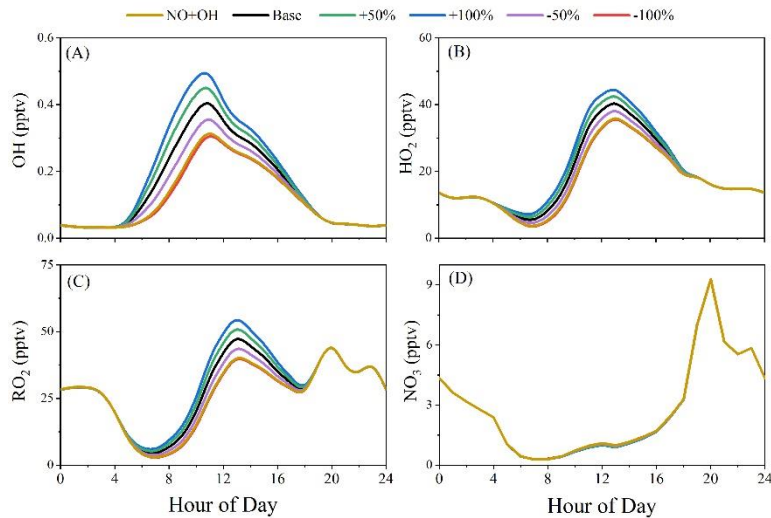
Figure 9: Simulated concentrations of (A): OH, (B): HO_2, (C): RO_2, and (D): NO_3. Different colored lines show results in different
450 **scenarios (NO + OH: only with the homogeneous source; Base: constrained by the observed HONO; +50%: constrained by the observed HONO×1.5; +100%: constrained by the observed HONO×2; -50%: constrained by the observed HONO×0.5; -100%: constrained by HONO = 0).**

3.3.2 Radical Production/Loss Rates and Reactivity

Figure 10A and Figure 10B illustrate the production/loss rates of OH and NO_3, respectively. The total production rates of these
455   radicals were similar to their loss rates due to their short lifetimes and high reactivities. For OH (Figure 10A), its largest source
was the reaction of $HO_2 + NO$ (average contribution: 70%), which is part of the propagation cycle and which is not a radical
initiation source (Elshorbany et al., 2010). HONO photolysis was the second-largest OH source (average contribution: 11%),
and it is expected to be the largest primary OH source after subtracting OH loss through HONO + OH and NO + OH (see
Section 3.3.4). Reactions with NO_2, CO, and C_5H_8 acted as the top three OH sinks but did not dominate OH loss due to high
460   OH reactivity caused by various other reactions, particularly those with other VOCs (see below).

Figure 10C and S11A show the OH reactivity with different classes of pollutants and their relative contributions, respectively.
Total OH reactivity showed a small peak of 20 s^{-1} in the morning and then kept almost constant around 17 s^{-1}. Among different
classes of pollutants, the measured inorganics (ordered by OH reactivity contribution: $NO_2 > CO > NO > O_3 > HONO > SO_2 > H_2O_2$) contributed the largest to the OH reactivity with values in the range of 2.6 – 8.4 s^{-1}. Their total contribution was larger
465   in the morning (43%) due to high NO, NO_2, and CO levels (Figure 2) and decreased to 15% at noontime. Reactivities with the
measured alkanes, alkenes, aromatics, and OVOCs were 0.95 – 1.2 s^{-1}, 3.3 – 3.9 s^{-1}, 2.2 – 2.9 s^{-1}, and 1.65 – 1.9 s^{-1}, leading to
relative contributions of around 5 – 7%, 18 – 22%, 11 – 17%, and 9 – 12% throughout the whole day, respectively. Likewise,
C_5H_8 alone contributed 4% of the OH reactivity in the early morning (0.85 s^{-1}), and its contribution increased to 12% at
noontime (2.1 s^{-1}) as a result of high levels of C_5H_8 at noontime.

470
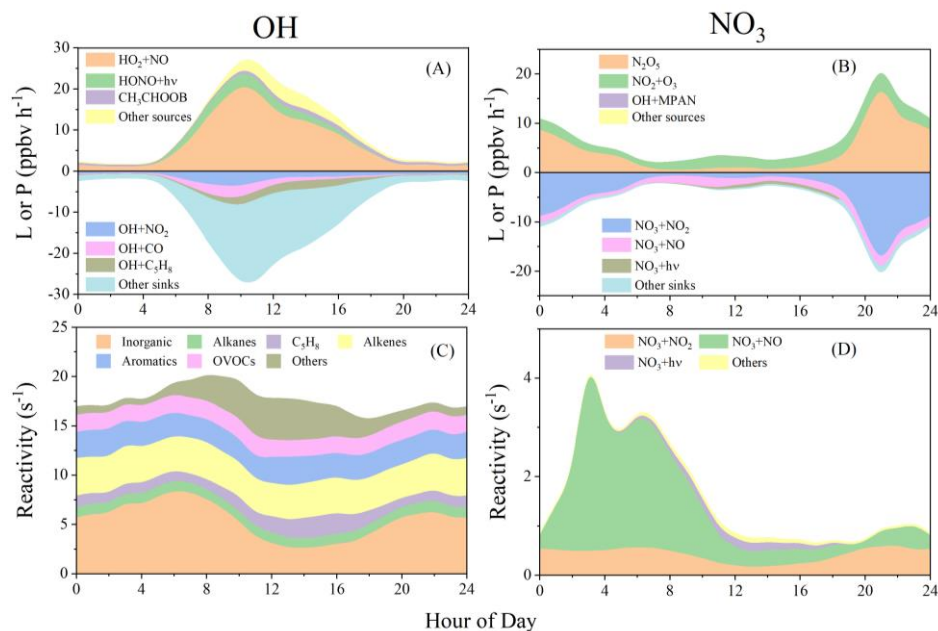
Figure 10: Production rates (P), loss rates (L) and reactivities of radicals. (A): L and P of OH; (B): L and P of NO_3; (C): Reactivities of OH and (D): Reactivities of NO_3. In (A) and (B), the top-3 sources or sinks are shown, and all the others are summarized in "Other sources" or "Other sinks". In (C), OH reactivities with different families of the measured species are shown

and reactivities with all the unmeasured species are summarized in "Others". In (D), NO_3 reactivities from top-3 reactions are shown and all the others are summarized in "Others".

Figure 10D and S11B show NO_3 reactivity with different pollutant classes and their relative contributions, respectively. Compared with the total OH reactivity, the total NO_3 reactivity exhibited lower values and a different variation profile. It showed a minimum of 1 s^{-1} at noontime and increased to around 4 s^{-1} at 2:00. , The reaction $NO_2 + O_3$ (R-11) is the most important net NO_3 source. In contrast, NO_3 formation by the N_2O_5 deposition (R-17) is almost compensated by the same amount of NO_3 loss during N_2O_5 production (R-14). NO_3 loss was dominated by its photolysis and its reactions with NO during the daytime and reactions with NO_2 at night. More discussion on the NO_3 chemistry is presented in the following section.

3.3.3 NO_3 Chemistry

As shown in Figure 9D, high NO_3 levels (diurnal peak: 9.3 pptv, time-series peak: 22 pptv) were simulated by the model. High NO_3 concentrations, as well as high NO_3 reactivities (Figures 10D), generally appeared at night (18:00 to 4:00 in the next day) when OH was very low and NO_3 was not lost by photolysis, indicating that the NO_3-initialized chemistry may play an important role in night-time chemistry at this site. To verify this assumption, we compared the C_5H_8 oxidation and nitrate formation through NO_3-induced reactions with other reactions.

3.3.3.1 C_5H_8 Oxidation

Figure 11 shows (A): the C_5H_8 loss rates (L(C_5H_8)) through different oxidation paths and (B): their relative contributions. L(C_5H_8) through O_3 was generally in the range of 0.04-0.12 ppbv h^{-1}. L(C_5H_8) through OH showed high values in the daytime and low ones during night. On the contrary to OH, loss rats L(C_5H_8) through NO_3 were low in the daytime and high during night. On average, L(C_5H_8) through OH, O_3, and NO_3 oxidation were 1.3, 0.07, and 0.16 ppbv h^{-1}, with relative contributions of 84%, 5%, and 11%, respectively. During the daytime, L(C_5H_8) through OH oxidation was generally one order of magnitude higher than those through NO_3 or O_3 oxidation, leading to a dominated C_5H_8 loss contribution of generally >90% through OH oxidation (Figure 11B). However, at night, OH was much lower and NO_3 was higher due to the absence of photochemistry, resulting in an increasing contribution of L(C_5H_8) through NO_3 oxidation (Figure 11B). Average L(C_5H_8) through night-time NO_3 oxidation increased to 0.30 ppbv h^{-1}, but L(C_5H_8) through OH oxidation decreased to 0.33 ppbv h^{-1}, resulting in a relatively high contribution of NO_3 oxidation (32 – 57%). NO_3 oxidation contributed to 44% of the night-time C_5H_8 loss, which is comparable to OH oxidation (48%) and much higher than O_3 oxidation (8%). C_5H_8 is an important common hemiterpene emitted by many species of vegetation and its oxidation plays a key role in secondary organic aerosol (SOA) formation. The results of the present study show that daytime OH-induced C_5H_8 oxidation is the most important, while NO_3-induced oxidation of C_5H_8 may also significantly affect the SOA formation during the night-time (Brown and Stutz, 2012; Mellouki et al., 2021).
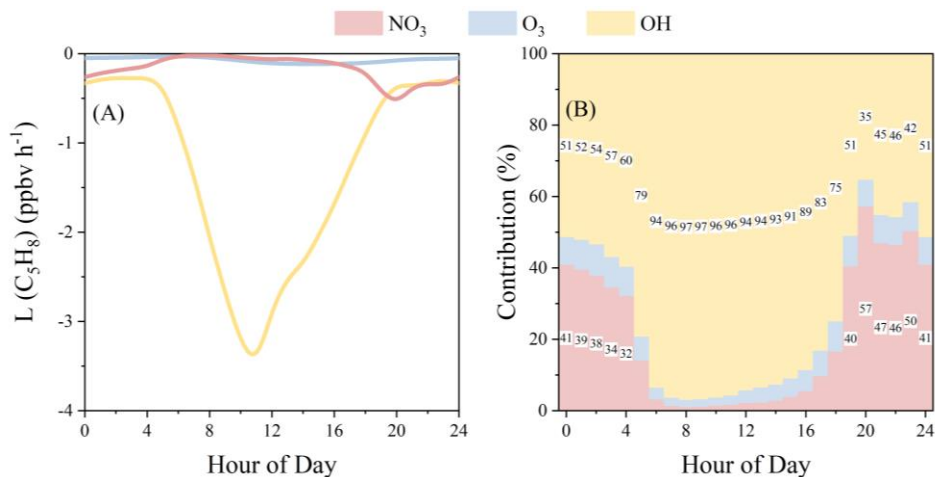
505 **Figure 11: (A): Diurnal loss rate of C_5H_8 by NO_3, O_3 and OH oxidation and (B): their diurnal relative contributions.**

3.3.3.2 HNO₃ Formation

As an important component of particulate matter, inorganic nitrate (pNO_3) is produced by the partitioning of gas-phase HNO_3 and by heterogeneous uptake of N_2O_5. HNO_3 formation from $OH+NO_2$ and from N_2O_5 hydrolysis on the aqueous aerosol surface are also the major daytime and night-time sinks for removing NO_x from the atmosphere. Hence, the production of

510 HNO_3, defined as $P(HNO_3) = P(HNO_3)_{OH} + P(HNO_3)_{NO_3}$, represents the upper limits of pNO_3 production. $P(HNO_3)_{OH}$ denotes the HNO_3 production through (R-18) in the model (Sce-0). For calculation of $P(HNO_3)_{NO_3}$, both HNO_3 formation through N_2O_5 heterogeneous uptake on the aerosol surface (R-16) and other NO_3-induced reactions were considered (the former is the dominant one).

$$NO_2 + OH \rightarrow HNO_3 \qquad \text{(R-18)}$$

515 In the model, parameterization for the heterogeneous N_2O_5 uptake is described by (Eq-9).

$$P(HNO_3)_{N_2O_5} = \frac{v(N_2O_5) \times S_a \times [N_2O_5]}{4} \times \gamma_{N_2O_5} \times 2, \qquad \text{(Eq-9)}$$

where $v(N_2O_5)$, $[N_2O_5]$, and $\gamma_{N_2O_5}$ represent the molecular speed, concentration, and heterogeneous uptake coefficient of N_2O_5, respectively. $\gamma_{N_2O_5}$ was typically set as 0.1 reported in previous studies (Brown and Stutz, 2012; Wang et al., 2017).

As shown in Figure 12, the overall $P(HNO_3)$ was high during the daytime and low during the night. During the daytime,

520 $P(HNO_3)_{NO_3}$ was generally much lower than $P(HNO_3)_{OH}$, leading to high contributions of $P(HNO_3)_{OH}$ (>90%). However, during the night, $P(HNO_3)_{OH}$ and its relative contribution to $P(HNO_3)$ remarkably increased. On average throughout all day, $P(HNO_3)_{NO_3}$ contributed 18%, significantly lower than $P(HNO_3)_{OH}$ (82%). However, at night, $P(HNO_3)_{NO_3}$ contribution increased to 51%, slightly higher than $P(HNO_3)_{OH}$ (49%). Model results may have uncertainties but shed light on the atmospheric chemistry in this polluted region. By far, very few NO_3 measurements are available in China (Lu et al., 2019;

525 Suhail et al., 2019), while its high concentration and important role in chemical oxidation presented in this study indicate the

necessity of direct NO_3 (as well as related species such as N_2O_5, $ClNO_2$, etc.) measurements in the NCP, where summertime O_3 levels are substantially increasing (Han et al., 2020; Li et al., 2019; Sun et al., 2016, 2019).
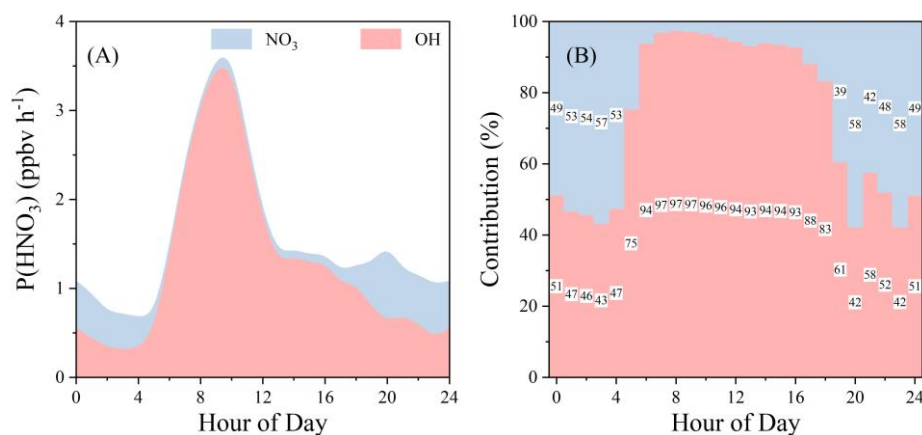
Figure 12: (A): HNO₃ production (P(HNO₃)) from NO₃- or OH- induced reactions and (B): their relative contribution at each hour of the day. NO₃-induced reactions include heterogeneous uptake of N₂O₅ on the aerosol surface and all the other NO₃ reactions that produce HNO₃.

3.3.4 Radical Initiation vs. Termination

Measurements of other radical precursors, such as H_2O_2 (through photolysis to produce OH), HCHO (through photolysis to produce HO_2), and alkenes (through ozonolysis via Criegee intermediate to produce OH, HO_2, and RO_2), were available, which allows a comparison of radical initiation (primary production) and termination ($T(RO_x)$). As shown in Figure 13, the overall radical initiation and termination showed similar variations and levels. Both, the sum of the RO_x initiation and termination showed peaks of about 7.6 ppbv h^{-1} at noon, which are in the range of 2.5-12.2 ppbv h^{-1} reported in previous studies (Elshorbany et al., 2010, 2012; Hofzumahaus et al., 2009; Kukui et al., 2014; Liu et al., 2012; Ren et al., 2003). During the daytime, it is evident that HONO photolysis ($P(RO_x)_{HONO\_net}$) made the largest contribution (20 – 70%, Figure 13B) to RO_x initiation, with an average of 37% (or 32% for all-day, Figure S12), followed by ozonolysis (29%), O_3 photolysis (21%), HCHO photolysis (13%), and H_2O_2 photolysis (1%). In particular, RO_x production from the ozonolysis of alkenes was significantly lower than that from HONO during 6:00 – 14:00 until later after 17:00 when it started to dominate RO_x production. At night with the absence of photochemistry, ozonolysis was the major source for primary RO_x. Due to the also high production of radicals during the daytime, ozonolysis played an important role in primary RO_x production (39% for all day). The termination of radicals $T(RO_x)$ was dominated by $NO_2 + OH \rightarrow HNO_3$, $NO_2 + CH_3COO_2 \rightarrow PAN$, and $HO_2 + HO_2 \rightarrow H_2O_2$ (Elshorbany et al., 2010, 2012; Hofzumahaus et al., 2009; Kukui et al., 2014; Liu et al., 2012; Stone et al., 2012).
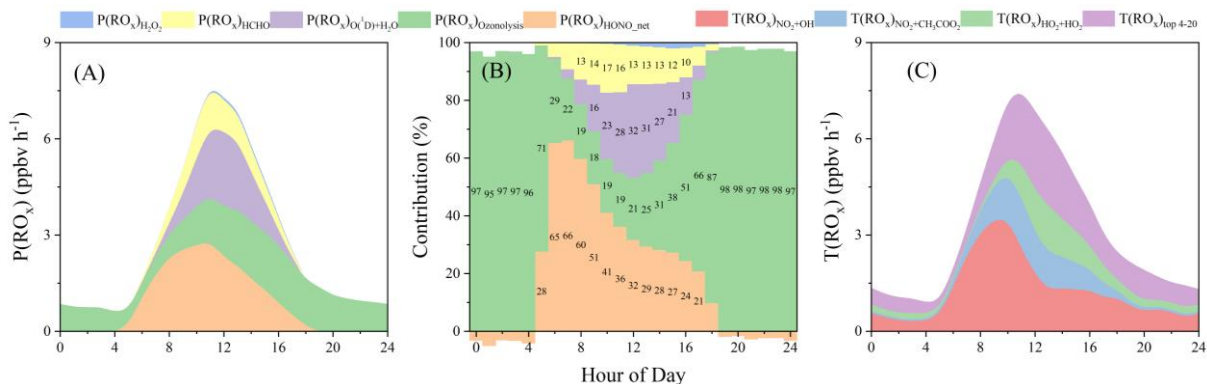
Figure 13: Primary RO$_x$ production and net RO$_x$ loss. (A): Production from different sources and (B): their relative contributions at different hours of the day. (C): the top-20 RO$_x$ loss rates. Note that the top-20 net radical loss paths were summarized here. It could represent the majority of total T(RO$_x$) as others (<0.03 ppbv h^{-1}) were at least 2 orders of magnitude lower than the sum of top-20. Night-time P(RO$_x$)$_{HONO\_net}$ was negative (a net sink for OH) so that its contribution was also negative at night. The same amounts of radical loss or production from equilibrium reactions (e.g., HO$_2$ + NO$_2$ ↔ HNO$_4$; CH$_3$COO$_2$ + NO$_2$ ↔ PAN) was excluded from radical initiation or termination. T(RO$_x$)$_{NO2+CH3COO2}$ represents the net PAN formation.

4. Summary

Atmospheric HONO and related parameters (VOCs, NO$_x$, PM$_{2.5}$, J(NO$_2$), etc.) were measured at the foot and the summit of Mt. Tai in the summer of 2018. The present study was conducted mainly based on measurements at the foot station. The observed HONO varied from 0.05 to about 3 ppbv, with an average of 0.62 ± 0.42 ppbv. With the implementation of a 0-D box model (F0AM) coupled with the Master Chemical Mechanism (MCM v3.3.1), the HONO budget and the radical (RO$_x$ + NO$_3$) chemistry were explored.

The main conclusions are summarized as follows:

1. The default HONO source, NO + OH, significantly underestimated the observed HONO concentrations. This reaction could only account for 13% of the observed HONO, revealing a strong unknown source (P$_{unknown}$). The diurnal profile of P$_{unknown}$ rapidly increased in the morning and peaked nearly 3 ppbv h^{-1} at ca. 1 hour before noon, suggesting additional photo-enhanced HONO formation processes.

2. A HONO/NO$_x$ ratio of 0.7% was derived for direct emission, and its contribution (15 – 25% at night but negligible during the daytime) was quantified by a new method developed in this study. Based on the constraints on the aerosol-derived HONO sources (NO$_2$ uptake on the aerosol surface and nitrate photolysis) obtained from the summit measurement (see the companion paper) and from recent laboratory studies, we found that the aerosol-derived HONO sources may not significantly contribute to HONO formation at the ground level. Their contributions to HONO formation were always smaller than NO + OH. Heterogeneous NO$_2$ conversion on the ground surface made the largest contribution to P$_{unknown}$, but it was sensitive to the MLH used for its parameterization. This addressed the importance of a reasonable MLH for exploring ground-level HONO formation in 0-D models and the necessity of vertical measurements.

3. HONO played an important role in RO_x but a negligible role in NO_3 concentrations. OH dominated the atmospheric oxidizing capacity in the daytime, while NO_3 appeared to be significant at night. Peaks of NO_3 time series and diurnal variation reached 22 and 9 pptv, respectively. NO_3 induced reactions contribute 18% of nitrate formation potential and 11% of the C_5H_8 oxidation throughout the whole day. While at night, NO_3 chemistry led to 51% and 44% of the nitrate formation potential and the C_5H_8 oxidation, respectively. NO_3 chemistry may significantly affect night-time secondary organic and inorganic aerosol formation in this high O_3 region. Hence, the direct measurement of NO_3 (along with HO_x, N_2O_5, $ClNO_2$, etc.) in this region should be conducted.

Acknowledgment

We are grateful to Shuyu Sun for her help with OVOCs measurements. We thank all researchers involved in this campaign from the Research Centre for Eco-Environmental Sciences-Chinese Academy of Sciences, Fudan University, Shandong Jianzhu University, Shandong University, and the Municipal Environmental Protection Bureau of Tai'an. C.X. thanks the University of Leeds for providing the MCM v3.3.1 and Glenn M. Wolfe for providing the F0AM platform.

Funding: This work was supported by the National Natural Science Foundation of China (Nos. 91544211, 41727805, 41931287, and 41975164), and the PIVOTS project provided by the Region Centre − Val de Loire (ARD 2020 program and CPER 2015 − 2020).

Author Contribution: C.X., C.Y., W.Z., X.H., P.L., C.Z., X.Z., C.L., Z.M., J.L., and J.W. performed the field measurements. C.X. analyzed the observation data, performed model simulations, and wrote the paper with input from all co-authors. C.Y. and J.K. also contributed by fruitful discussions and comments on model simulations and writing. J.K., C.Y., K.L., V.C., A.M., and Y.M. revised the manuscript.

Competing Interests: The authors declare no competing financial interest.

Data Availability: All the data used in this study is available upon request from the corresponding authors.

References

Acker, K., Febo, A., Trick, S., Perrino, C., Bruno, P., Wiesen, P., Möller, D., Wieprecht, W., Auel, R., Giusto, M., Geyer, A., Platt, U. and Allegrini, I.: Nitrous acid in the urban area of Rome, Atmos. Environ., 40(17), 3123–3133, doi:10.1016/j.atmosenv.2006.01.028, 2006.

Alicke, B., Platt, U. and Stutz, J.: Impact of nitrous acid photolysis on the total hydroxyl radical budget during the Limitation of Oxidant Production/Pianura Padana Produzione di Ozono study in Milan, J. Geophys. Res. Atmos., 107(D22), 8196, doi:10.1029/2000JD000075, 2002.

Alicke, B., Geyer, A., Hofzumahaus, A., Holland, F., Konrad, S., Pätz, H.-W., Schäfer, J., Stutz, J., Volz-Thomas, A. and Platt, U.: OH formation by HONO photolysis during the BERLIOZ experiment, J. Geophys. Res. Atmos., 108(D4), 8247, doi:10.1029/2001JD000579, 2003.

Brown, S. S. and Stutz, J.: Nighttime radical observations and chemistry, Chem. Soc. Rev., 41(19), 6405–6447, doi:10.1039/c2cs35181a, 2012.

Brown, S. S., Thornton, J. A., Keene, W. C., Pszenny, A. A. P., Sive, B. C., Dubé, W. P., Wagner, N. L., Young, C. J., Riedel, T. P., Roberts, J. M., Vandenboer, T. C., Bahreini, R., Öztürk, F., Middlebrook, A. M., Kim, S., Hübler, G. and Wolfe, D. E.: Nitrogen, Aerosol Composition, and Halogens on a Tall Tower (NACHTT): Overview of a wintertime air chemistry field study in the front range urban corridor of Colorado, J. Geophys. Res. Atmos., 118(14), 8067–8085, doi:10.1002/jgrd.50537, 2013.

Carslaw, D. C. and Beevers, S. D.: Estimations of road vehicle primary NO_2 exhaust emission fractions using monitoring data in London, Atmos. Environ., 39(1), 167–177, doi:10.1016/j.atmosenv.2004.08.053, 2005.

Chen, Q., Edebeli, J., McNamara, S. M., Kulju, K. D., May, N. W., Bertman, S. B., Thanekar, S., Fuentes, J. D. and Pratt, K. A.: HONO, Particulate Nitrite, and Snow Nitrite at a Midlatitude Urban Site during Wintertime, ACS Earth Sp. Chem., 3(5), 811–822, doi:10.1021/acsearthspacechem.9b00023, 2019.

Crilley, L. R., Kramer, L. J., Ouyang, B., Duan, J., Zhang, W., Tong, S., Ge, M., Tang, K., Qin, M., Xie, P., Shaw, M. D., Lewis, A. C., Mehra, A., Bannan, T. J., Worrall, S. D., Priestley, M., Bacak, A., Coe, H., Allan, J., Percival, C. J., Popoola, O. A. M., Jones, R. L. and Bloss, W. J.: Intercomparison of nitrous acid (HONO) measurement techniques in a megacity (Beijing), Atmos. Meas. Tech., 12(12), 6449–6463, doi:10.5194/amt-12-6449-2019, 2019.

Elshorbany, Y. F., Kurtenbach, R., Wiesen, P., Lissi, E., Rubio, M., Villena, G., Gramsch, E., Rickard, A. R., Pilling, M. J. and Kleffmann, J.: Oxidation capacity of the city air of Santiago, Chile, Atmos. Chem. Phys., 9(6), 2257–2273, doi:10.5194/acp-9-2257-2009, 2009.

Elshorbany, Y. F., Kleffmann, J., Kurtenbach, R., Lissi, E., Rubio, M., Villena, G., Gramsch, E., Rickard, A. R., Pilling, M. J. and Wiesen, P.: Seasonal dependence of the oxidation capacity of the city of Santiago de Chile, Atmos. Environ., 44(40), 5383–5394, doi:10.1016/j.atmosenv.2009.08.036, 2010.

Elshorbany, Y. F., Kleffmann, J., Hofzumahaus, A., Kurtenbach, R., Wiesen, P., Brauers, T., Bohn, B., Dorn, H.-P., Fuchs, H., Holland, F., Rohrer, F., Tillmann, R., Wegener, R., Wahner, A., Kanaya, Y., Yoshino, A., Nishida, S., Kajii, Y., Martinez, M., Kubistin, D., Harder, H., Lelieveld, J., Elste, T., Plass-Dümer, C., Stange, G., Berresheim, H. and Schurath, U.: HO_x budgets during HOxComp: A case study of HO_x chemistry under NO_x-limited conditions, J. Geophys. Res. Atmos., 117(3), D03307, doi:10.1029/2011JD017008, 2012.

Finlayson-Pitts, B. J., Wingen, L. M., Sumner, A. L., Syomin, D. and Ramazan, K. A.: The heterogeneous hydrolysis of NO_2

635   in laboratory systems and in outdoor and indoor atmospheres: An integrated mechanism, Phys. Chem. Chem. Phys., 5(2),

223–242, doi:10.1039/b208564j, 2003.

George, C., Strekowski, R. S., Kleffmann, J., Stemmler, K. and Ammann, M.: Photoenhanced uptake of gaseous NO_2 on

solid organic compounds: a photochemical source of HONO?, Faraday Discuss., 130, 195–210, doi:10.1039/b417888m,

2005.

640   Han, C., Yang, W., Wu, Q., Yang, H. and Xue, X.: Heterogeneous Photochemical Conversion of NO_2 to HONO on the

Humic Acid Surface under Simulated Sunlight, Environ. Sci. Technol., 50(10), 5017–5023, doi:10.1021/acs.est.5b05101,

2016.

Han, S., Yao, Q., Tie, X., Zhang, Y., Zhang, M., Li, P. and Cai, Z.: Analysis of surface and vertical measurements of O_3 and

its chemical production in the NCP region, China, Atmos. Environ., 241, 117759, doi:10.1016/j.atmosenv.2020.117759,

645   2020.

He, L., Zhang, S., Hu, J., Li, Z., Zheng, X., Cao, Y., Xu, G., Yan, M. and Wu, Y.: On-road emission measurements of

reactive nitrogen compounds from heavy-duty diesel trucks in China, Environ. Pollut., 262, 114280,

doi:10.1016/j.envpol.2020.114280, 2020.

Heard, D. E., Carpenter, L. J., Creasey, D. J., Hopkins, J. R., Lee, J. D., Lewis, A. C., Pilling, M. J., Seakins, P. W., Carslaw,

650   N. and Emmerson, K. M.: High levels of the hydroxyl radical in the winter urban troposphere, Geophys. Res. Lett., 31(18),

doi:10.1029/2004GL020544, 2004.

Heland, J., Kleffmann, J., Kurtenbach, R. and Wiesen, P.: A New Instrument To Measure Gaseous Nitrous Acid (HONO) in

the Atmosphere, Environ. Sci. Technol., 35(15), 3207–3212, doi:10.1021/es000303t, 2001.

Hendrick, F., Müller, J.-F., Clémer, K., Wang, P., De Mazière, M., Fayt, C., Gielen, C., Hermans, C., Ma, J. Z., Pinardi, G.,

655   Stavrakou, T., Vlemmix, T. and Van Roozendael, M.: Four years of ground-based MAX-DOAS observations of HONO and

NO_2 in the Beijing area, Atmos. Chem. Phys., 14(2), 765–781, doi:10.5194/acp-14-765-2014, 2014.

Hofzumahaus, A., Rohrer, F., Lu, K., Bohn, B., Brauers, T., Chang, C.-C., Fuchs, H., Holland, F., Kita, K., Kondo, Y., Li,

X., Lou, S., Shao, M., Zeng, L., Wahner, A. and Zhang, Y.: Amplified trace gas removal in the troposphere, Science,

324(5935), 1702–1704, doi:10.1126/science.1164566, 2009.

660   Jenkin, M. E., Saunders, S. M. and Pilling, M. J.: The tropospheric degradation of volatile organic compounds: a protocol for

mechanism development, Atmos. Environ., 31(1), 81–104, doi:10.1016/S1352-2310(96)00105-7, 1997.

Kanaya, Y., Pochanart, P., Liu, Y., Li, J., Tanimoto, H., Kato, S., Suthawaree, J., Inomata, S., Taketani, F., Okuzawa, K.,

Kawamura, K., Akimoto, H. and Wang, Z. F.: Rates and regimes of photochemical ozone production over Central East

China in June 2006: A box model analysis using comprehensive measurements of ozone precursors, Atmos. Chem. Phys., 9(20), 7711–7723, doi:10.5194/acp-9-7711-2009, 2009.

Kanaya, Y., Akimoto, H., Wang, Z.-F., Pochanart, P., Kawamura, K., Liu, Y., Li, J., Komazaki, Y., Irie, H., Pan, X.-L., Taketani, F., Yamaji, K., Tanimoto, H., Inomata, S., Kato, S., Suthawaree, J., Okuzawa, K., Wang, G., Aggarwal, S. G., Fu, P. Q., Wang, T., Gao, J., Wang, Y. and Zhuang, G.: Overview of the Mount Tai Experiment (MTX2006) in central East China in June 2006: Studies of significant regional air pollution, Atmos. Chem. Phys., 13(16), 8265–8283, doi:10.5194/acp-13-8265-2013, 2013.

Kirchstetter, T. W., Harley, R. A. and Littlejohn, D.: Measurement of nitrous acid in motor vehicle exhaust, Environ. Sci. Technol., 30(9), 2843–2849, doi:10.1021/es960135y, 1996.

Kleffmann, J.: Daytime sources of nitrous acid (HONO) in the atmospheric boundary layer, ChemPhysChem, 8(8), 1137–1144, doi:10.1002/cphc.200700016, 2007.

Kleffmann, J., Kurtenbach, R., Lörzer, J., Wiesen, P., Kalthoff, N., Vogel, B. and Vogel, H.: Measured and simulated vertical profiles of nitrous acid - Part I: Field measurements, Atmos. Environ., 37(21), 2949–2955, doi:10.1016/S1352-2310(03)00242-5, 2003.

Kleffmann, J., Gavriloaiei, T., Hofzumahaus, A., Holland, F., Koppmann, R., Rupp, L., Schlosser, E., Siese, M. and Wahner, A.: Daytime formation of nitrous acid: A major source of OH radicals in a forest, Geophys. Res. Lett., 32(5), L05818, doi:10.1029/2005GL022524, 2005.

Kleffmann, J., Lörzer, J. C., Wiesen, P., Kern, C., Trick, S., Volkamer, R., Rodenas, M. and Wirtz, K.: Intercomparison of the DOAS and LOPAP techniques for the detection of nitrous acid (HONO), Atmos. Environ., 40(20), 3640–3652, doi:10.1016/j.atmosenv.2006.03.027, 2006.

Kramer, L. J., Crilley, L. R., Adams, T. J., Ball, S. M., Pope, F. D. and Bloss, W. J.: Nitrous acid (HONO) emissions under real-world driving conditions from vehicles in a UK road tunnel, Atmos. Chem. Phys., 20(9), 5231–5248, doi:10.5194/acp-20-5231-2020, 2020.

Kukui, A., Legrand, M., Preunkert, S., Frey, M. M., Loisil, R., Gil Roca, J., Jourdain, B., King, M. D., France, J. L. and Ancellet, G.: Measurements of OH and RO_2 radicals at Dome C, East Antarctica, Atmos. Chem. Phys., 14(22), 12373–12392, doi:10.5194/acp-14-12373-2014, 2014.

Kurtenbach, R., Becker, K. H., Gomes, J. A. G., Kleffmann, J., Lörzer, J. C., Spittler, M., Wiesen, P., Ackermann, R., Geyer, A. and Platt, U.: Investigations of emissions and heterogeneous formation of HONO in a road traffic tunnel, Atmos. Environ., 35(20), 3385–3394, doi:10.1016/S1352-2310(01)00138-8, 2001.

Kurtenbach, R., Kleffmann, J., Niedojadlo, A. and Wiesen, P.: Primary NO_2 emissions and their impact on air quality in traffic environments in Germany, Environ. Sci. Eur., 24(21), 1–8, doi:10.1186/2190-4715-24-21, 2012.

695 Laufs, S. and Kleffmann, J.: Investigations on HONO formation from photolysis of adsorbed HNO_3 on quartz glass surfaces, Phys. Chem. Chem. Phys., 18(14), 9616–9625, doi:10.1039/c6cp00436a, 2016.

Lee, J. D., Whalley, L. K., Heard, D. E., Stone, D., Dunmore, R. E., Hamilton, J. F., Young, D. E., Allan, J. D., Laufs, S. and Kleffmann, J.: Detailed budget analysis of HONO in central London reveals a missing daytime source, Atmos. Chem. Phys., 16(5), 2747–2764, doi:10.5194/acp-16-2747-2016, 2016.

700 Legrand, M., Preunkert, S., Frey, M., Bartels-Rausch, T., Kukui, A., King, M. D., Savarino, J., Kerbrat, M. and Jourdain, B.: Large mixing ratios of atmospheric nitrous acid (HONO) at Concordia (East Antarctic Plateau) in summer: A strong source from surface snow?, Atmos. Chem. Phys., 14(18), 9963–9976, doi:10.5194/acp-14-9963-2014, 2014.

Li, D., Xue, L., Wen, L., Wang, X., Chen, T., Mellouki, A., Chen, J. and Wang, W.: Characteristics and sources of nitrous acid in an urban atmosphere of northern China: Results from 1-yr continuous observations, Atmos. Environ., 182, 296–306, 705 doi:10.1016/j.atmosenv.2018.03.033, 2018.

Li, G., Lei, W., Zavala, M., Volkamer, R., Dusanter, S., Stevens, P. and Molina, L. T.: Impacts of HONO sources on the photochemistry in Mexico City during the MCMA-2006/MILAGO Campaign, Atmos. Chem. Phys., 10(14), 6551–6567, doi:10.5194/acp-10-6551-2010, 2010.

Li, K., Jacob, D. J., Liao, H., Shen, L., Zhang, Q. and Bates, K. H.: Anthropogenic drivers of 2013–2017 trends in summer 710 surface ozone in China, Proc. Natl. Acad. Sci. U. S. A., 116(2), 422–427, doi:10.1073/pnas.1812168116, 2019.

Li, X., Brauers, T., Häseler, R., Bohn, B., Fuchs, H., Hofzumahaus, A., Holland, F., Lou, S., Lu, K. D., Rohrer, F., Hu, M., Zeng, L. M., Zhang, Y. H., Garland, R. M., Su, H., Nowak, A., Wiedensohler, A., Takegawa, N., Shao, M. and Wahner, A.: Exploring the atmospheric chemistry of nitrous acid (HONO) at a rural site in Southern China, Atmos. Chem. Phys., 12(3), 1497–1513, doi:10.5194/acp-12-1497-2012, 2012.

715 Liu, C., Mu, Y., Zhang, C., Zhang, Z., Zhang, Y., Liu, J., Sheng, J. and Quan, J.: Development of gas chromatography-flame ionization detection system with a single column and liquid nitrogen-free for measuring atmospheric C_2–C_{12} hydrocarbons, J. Chromatogr. A, 1427, 134–141, doi:10.1016/j.chroma.2015.11.060, 2016.

Liu, P., Ye, C., Xue, C., Zhang, C., Mu, Y. and Sun, X.: Formation mechanisms of atmospheric nitrate and sulfate during the winter haze pollution periods in Beijing: gas-phase, heterogeneous and aqueous-phase chemistry, Atmos. Chem. Phys., 720 20(7), 4153–4165, doi:10.5194/acp-20-4153-2020, 2020.

Liu, Y., Lu, K., Ma, Y., Yang, X., Zhang, W., Wu, Y., Peng, J., Shuai, S., Hu, M. and Zhang, Y.: Direct emission of nitrous acid (HONO) from gasoline cars in China determined by vehicle chassis dynamometer experiments, Atmos. Environ., 169, 89–96, doi:10.1016/j.atmosenv.2017.07.019, 2017a.

725 Liu, Y., Lu, K., Ma, Y., Yang, X., Zhang, W., Wu, Y., Peng, J., Shuai, S., Hu, M. and Zhang, Y.: Direct emission of nitrous acid (HONO) from gasoline cars in China determined by vehicle chassis dynamometer experiments, Atmos. Environ., 169, 89–96, doi:10.1016/j.atmosenv.2017.07.019, 2017b.

Liu, Y., Lu, K., Li, X., Dong, H., Tan, Z., Wang, H., Zou, Q., Wu, Y., Zeng, L., Hu, M., Min, K.-E., Kecorius, S., Wiedensohler, A. and Zhang, Y.: A Comprehensive Model Test of the HONO Sources Constrained to Field Measurements at Rural North China Plain, Environ. Sci. Technol., 53(7), 3517–3525, doi:10.1021/acs.est.8b06367, 2019.

730 Liu, Z., Wang, Y., Gu, D., Zhao, C., Huey, L. G., Stickel, R., Liao, J., Shao, M., Zhu, T., Zeng, L., Amoroso, A., Costabile, F., Chang, C.-C. and Liu, S.-C.: Summertime photochemistry during CAREBeijing-2007: RO_x budgets and O_3 formation, Atmos. Chem. Phys., 12(16), 7737–7752, doi:10.5194/acp-12-7737-2012, 2012.

Lu, K., Guo, S., Tan, Z., Wang, H., Shang, D., Liu, Y., Li, X., Wu, Z., Hu, M. and Zhang, Y.: Exploring atmospheric free-radical chemistry in China: the self-cleansing capacity and the formation of secondary air pollution, Natl. Sci. Rev., 6(3), 735 579–594, doi:10.1093/nsr/nwy073, 2019.

Mellouki, A., Ammann, M., Cox, R. A., Crowley, J. N., Herrmann, H., Jenkin, M. E., McNeill, V. F., Troe, J. and Wallington, T. J.: Evaluated kinetic and photochemical data for atmospheric chemistry: volume VIII – gas-phase reactions of organic species with four, or more, carbon atoms (≥ C4), Atmos. Chem. Phys., 21(6), 4797–4808, doi:10.5194/acp-21-4797-2021, 2021.

740 Meng, F., Qin, M., Tang, K., Duan, J., Fang, W., Liang, S., Ye, K., Xie, P., Sun, Y., Xie, C., Ye, C., Fu, P., Liu, J. and Liu, W.: High-resolution vertical distribution and sources of HONO and NO_2 in the nocturnal boundary layer in urban Beijing, China, Atmos. Chem. Phys., 20(8), 5071–5092, doi:10.5194/acp-20-5071-2020, 2020.

Meusel, H., Kuhn, U., Reiffs, A., Mallik, C., Harder, H., Martinez, M., Schuladen, J., Bohn, B., Parchatka, U., Crowley, J. N., Fischer, H., Tomsche, L., Novelli, A., Hoffmann, T., Janssen, R. H. H., Hartogensis, O., Pikridas, M., Vrekoussis, M., 745 Bourtsoukidis, E., Weber, B., Lelieveld, J., Williams, J., Pöschl, U., Cheng, Y. and Su, H.: Daytime formation of nitrous acid at a coastal remote site in Cyprus indicating a common ground source of atmospheric HONO and NO, Atmos. Chem. Phys., 16(22), 14475–14493, doi:10.5194/acp-16-14475-2016, 2016.

Michoud, V., Kukui, A., Camredon, M., Colomb, A., Borbon, A., Miet, K., Aumont, B., Beekmann, M., Durand-Jolibois, R., Perrier, S., Zapf, P., Siour, G., Ait-Helal, W., Locoge, N., Sauvage, S., Afif, C., Gros, V., Furger, M., Ancellet, G. and 750 Doussin, J. F.: Radical budget analysis in a suburban European site during the MEGAPOLI summer field campaign, Atmos. Chem. Phys., 12(24), 11951–11974, doi:10.5194/acp-12-11951-2012, 2012.

Michoud, V., Colomb, A., Borbon, A., Miet, K., Beekmann, M., Camredon, M., Aumont, B., Perrier, S., Zapf, P., Siour, G., Ait-Helal, W., Afif, C., Kukui, A., Furger, M., Dupont, J. C., Haeffelin, M. and Doussin, J. F.: Study of the unknown HONO daytime source at a European suburban site during the MEGAPOLI summer and winter field campaigns, Atmos. Chem.

755   Phys., 14(6), 2805–2822, doi:10.5194/acp-14-2805-2014, 2014.

Neuman, J. A., Trainer, M., Brown, S. S., Min, K.-E., Nowak, J. B., Parrish, D. D., Peischl, J., Pollack, I. B., Roberts, J. M., Ryerson, T. B. and Veres, P. R.: HONO emission and production determined from airborne measurements over the Southeast U.S., J. Geophys. Res. Atmos., 121(15), 9237–9250, doi:10.1002/2016JD025197, 2016.

Oswald, R., Behrendt, T., Ermel, M., Wu, D., Su, H., Cheng, Y., Breuninger, C., Moravek, A., Mougin, E., Delon, C.,

760   Loubet, B., Pommerening-Röser, A., Sörgel, M., Pöschl, U., Hoffmann, T., Andreae, M. O., Meixner, F. X. and Trebs, I.: HONO emissions from soil bacteria as a major source of atmospheric reactive nitrogen, Science, 341(6151), 1233–1235, doi:10.1126/science.1242266, 2013.

Platt, U., Perner, D., Harris, G. W., Winer, A. M. and Pitts Jr, J. N.: Observations of nitrous acid in an urban atmosphere by differential optical absorption, Nature, 285(5763), 312–314, doi:10.1038/285312a0, 1980.

765   Qin, M., Xie, P.-H., Liu, W.-Q., Li, A., Dou, K., Fang, W., Liu, J.-G. and Zhang, W.-J.: Observation of atmospheric nitrous acid with DOAS in Beijing, China, J. Environ. Sci. (China), 18(1), 69–75, 2006.

Ren, X., Harder, H., Martinez, M., Lesher, R. L., Oliger, A., Simpas, J. B., Brune, W. H., Schwab, J. J., Demerjian, K. L., He, Y., Zhou, X. and Gao, H.: OH and HO_2 chemistry in the urban atmosphere of New York City, Atmos. Environ., 37(26), 3639–3651, doi:10.1016/S1352-2310(03)00459-X, 2003.

770   Roberts, J. M., Williams, J., Baumann, K., Buhr, M. P., Goldan, P. D., Holloway, J., Hübler, G., Kuster, W. C., McKeen, S. A., Ryerson, T. B., Trainer, M., Williams, E. J., Fehsenfeld, F. C., Bertman, S. B., Nouaime, G., Seaver, C., Grodzinsky, G., Rodgers, M. and Young, V. L.: Measurements of PAN, PPN, and MPAN made during the 1994 and 1995 Nashville Intensives of the Southern Oxidant Study: Implications for regional ozone production from biogenic hydrocarbons, J. Geophys. Res. Atmos., 103(D17), 22473–22490, doi:10.1029/98JD01637, 1998.

775   Rohrer, F. and Berresheim, H.: Strong correlation between levels of tropospheric hydroxyl radicals and solar ultraviolet radiation, Nature, 442(7099), 184–187, doi:10.1038/nature04924, 2006.

Rollins, A. W., Kiendler-Scharr, A., Fry, J. L., Brauers, T., Brown, S. S., Dorn, H. P., Dubé, W. P., Fuchs, H., Mensah, A., Mentel, T. F., Rohrer, F., Tillmann, R., Wegener, R., Wooldridge, P. J. and Cohen, R. C.: Isoprene oxidation by nitrate radical: alkyl nitrate and secondary organic aerosol yields, Atmos. Chem. Phys., 9(18), 6685–6703, doi:10.5194/acp-9-6685-

780   2009, 2009.

Romer, P. S., Wooldridge, P. J., Crounse, J. D., Kim, M. J., Wennberg, P. O., Dibb, J. E., Scheuer, E., Blake, D. R., Meinardi, S., Brosius, A. L., Thames, A. B., Miller, D. O., Brune, W. H., Hall, S. R., Ryerson, T. B. and Cohen, R. C.:

Constraints on Aerosol Nitrate Photolysis as a Potential Source of HONO and NO_x, Environ. Sci. Technol., 52(23), 13738–13746, doi:10.1021/acs.est.8b03861, 2018.

785 Sarwar, G., Roselle, S. J., Mathur, R., Appel, W., Dennis, R. L. and Vogel, B.: A comparison of CMAQ HONO predictions with observations from the Northeast Oxidant and Particle Study, Atmos. Environ., 42(23), 5760–5770, doi:10.1016/j.atmosenv.2007.12.065, 2008.

Scharko, N. K., Schütte, U. M. E., Berke, A. E., Banina, L., Peel, H. R., Donaldson, M. A., Hemmerich, C., White, J. R. and Raff, J. D.: Combined Flux Chamber and Genomics Approach Links Nitrous Acid Emissions to Ammonia Oxidizing
790 Bacteria and Archaea in Urban and Agricultural Soil, Environ. Sci. Technol., 49(23), 13825–13834, doi:10.1021/acs.est.5b00838, 2015.

Seinfeld, J. H. and Pandis, S. N.: Atmospheric Chemistry and Physics: From Air Pollution to Climate Change, John Wiley & Sons., 2016.

Shi, Q., Tao, Y., Krechmer, J. E., Heald, C. L., Murphy, J. G., Kroll, J. H. and Ye, Q.: Laboratory Investigation of
795 Renoxification from the Photolysis of Inorganic Particulate Nitrate, Environ. Sci. Technol., 55(2), 854–861, doi:10.1021/acs.est.0c06049, 2021.

Slater, E. J., Whalley, L. K., Woodward-Massey, R., Ye, C., Lee, J. D., Squires, F., Hopkins, J. R., Dunmore, R. E., Shaw, M., Hamilton, J. F., Lewis, A. C., Crilley, L. R., Kramer, L., Bloss, W., Vu, T., Sun, Y., Xu, W., Yue, S., Ren, L., Acton, W. J. F., Hewitt, C. N., Wang, X., Fu, P. and Heard, D. E.: Elevated levels of OH observed in haze events during wintertime in
800 central Beijing, Atmos. Chem. Phys., 20(23), 14847–14871, doi:10.5194/acp-20-14847-2020, 2020.

Sörgel, M., Regelin, E., Bozem, H., Diesch, J.-M., Drewnick, F., Fischer, H., Harder, H., Held, A., Hosaynali-Beygi, Z., Martinez, M. and Zetzsch, C.: Quantification of the unknown HONO daytime source and its relation to NO_2, Atmos. Chem. Phys., 11(20), 10433–10447, doi:10.5194/acp-11-10433-2011, 2011.

Spataro, F., Ianniello, A., Esposito, G., Allegrini, I., Zhu, T. and Hu, M.: Occurrence of atmospheric nitrous acid in the urban
805 area of Beijing (China), Sci. Total Environ., 447, 210–224, doi:10.1016/j.scitotenv.2012.12.065, 2013.

Stemmler, K., Ammann, M., Donders, C., Kleffmann, J. and George, C.: Photosensitized reduction of nitrogen dioxide on humic acid as a source of nitrous acid, Nature, 440(7081), 195–198, doi:10.1038/nature04603, 2006.

Stemmler, K., Ndour, M., Elshorbany, Y., Kleffmann, J., D'Anna, B., George, C., Bohn, B. and Ammann, M.: Light induced conversion of nitrogen dioxide into nitrous acid on submicron humic acid aerosol, Atmos. Chem. Phys., 7(16), 4237–4248,
810 doi:10.5194/acp-7-4237-2007, 2007.

Stone, D., Whalley, L. K. and Heard, D. E.: Tropospheric OH and HO_2 radicals: Field measurements and model comparisons, Chem. Soc. Rev., 41(19), 6348–6404, doi:10.1039/c2cs35140d, 2012.

Su, H., Cheng, Y. F., Shao, M., Gao, D. F., Yu, Z. Y., Zeng, L. M., Slanina, J., Zhang, Y. H. and Wiedensohler, A.: Nitrous acid (HONO) and its daytime sources at a rural site during the 2004 PRIDE-PRD experiment in China, J. Geophys. Res.
815 Atmos., 113(D14), D14312, doi:10.1029/2007JD009060, 2008.

Suhail, K., George, M., Chandran, S., Varma, R., Venables, D. S., Wang, M. and Chen, J.: Open path incoherent broadband cavity-enhanced measurements of NO_3 radical and aerosol extinction in the North China Plain, Spectrochim. Acta Part A Mol. Biomol. Spectrosc., 208, 24–31, doi:10.1016/j.saa.2018.09.023, 2019.

Sun, L., Xue, L., Wang, T., Gao, J., Ding, A., Cooper, O. R., Lin, M., Xu, P., Wang, Z., Wang, X., Wen, L., Zhu, Y., Chen,
820 T., Yang, L., Wang, Y., Chen, J. and Wang, W.: Significant increase of summertime ozone at Mount Tai in Central Eastern China, Atmos. Chem. Phys., 16(16), 10637–10650, doi:10.5194/acp-16-10637-2016, 2016.

Sun, L., Xue, L., Wang, Y., Li, L., Lin, J., Ni, R., Yan, Y., Chen, L., Li, J., Zhang, Q. and Wang, W.: Impacts of meteorology and emissions on summertime surface ozone increases over central eastern China between 2003 and 2015, Atmos. Chem. Phys., 19(3), 1455–1469, doi:10.5194/acp-19-1455-2019, 2019.

825 Tan, Z., Fuchs, H., Lu, K., Hofzumahaus, A., Bohn, B., Broch, S., Dong, H., Gomm, S., Häseler, R., He, L., Holland, F., Li, X., Liu, Y., Lu, S., Rohrer, F., Shao, M., Wang, B., Wang, M., Wu, Y., Zeng, L., Zhang, Y., Wahner, A. and Zhang, Y.: Radical chemistry at a rural site (Wangdu) in the North China Plain: Observation and model calculations of OH, HO_2 and RO_2 radicals, Atmos. Chem. Phys., 17(1), 663–690, doi:10.5194/acp-17-663-2017, 2017.

Tang, K., Qin, M., Duan, J., Fang, W., Meng, F., Liang, S., Xie, P., Liu, J., Liu, W., Xue, C. and Mu, Y.: A dual dynamic
830 chamber system based on IBBCEAS for measuring fluxes of nitrous acid in agricultural fields in the North China Plain, Atmos. Environ., 196, 10–19, doi:10.1016/j.atmosenv.2018.09.059, 2019.

Travis, K. R., Heald, C. L., Allen, H. M., Apel, E. C., Arnold, S. R., Blake, D. R., Brune, W. H., Chen, X., Commane, R., Crounse, J. D., Daube, B. C., Diskin, G. S., Elkins, J. W., Evans, M. J., Hall, S. R., Hintsa, E. J., Hornbrook, R. S., Kasibhatla, P. S., Kim, M. J., Luo, G., McKain, K., Millet, D. B., Moore, F. L., Peischl, J., Ryerson, T. B., Sherwen, T.,
835 Thames, A. B., Ullmann, K., Wang, X., Wennberg, P. O., Wolfe, G. M. and Yu, F.: Constraining remote oxidation capacity with ATom observations, Atmos. Chem. Phys., 20(13), 7753–7781, doi:10.5194/acp-20-7753-2020, 2020.

Vandenboer, T. C., Brown, S. S., Murphy, J. G., Keene, W. C., Young, C. J., Pszenny, A. A. P., Kim, S., Warneke, C., De Gouw, J. A., Maben, J. R., Wagner, N. L., Riedel, T. P., Thornton, J. A., Wolfe, D. E., Dubé, W. P., Öztürk, F., Brock, C. A., Grossberg, N., Lefer, B., Lerner, B., Middlebrook, A. M. and Roberts, J. M.: Understanding the role of the ground surface in
840 HONO vertical structure: High resolution vertical profiles during NACHTT-11, J. Geophys. Res. Atmos., 118(17), 10,155-10,171, doi:10.1002/jgrd.50721, 2013.

Villena, G., Kleffmann, J., Kurtenbach, R., Wiesen, P., Lissi, E., Rubio, M. A., Croxatto, G. and Rappenglück, B.: Vertical gradients of HONO, NO$_x$ and O$_3$ in Santiago de Chile, Atmos. Environ., 45(23), 3867–3873, doi:10.1016/j.atmosenv.2011.01.073, 2011.

845 Villena, G., Bejan, I., Kurtenbach, R., Wiesen, P. and Kleffmann, J.: Interferences of commercial NO$_2$ instruments in the urban atmosphere and in a smog chamber, Atmos. Meas. Tech., 5(1), 149–159, doi:10.5194/amt-5-149-2012, 2012.

Vogel, B., Vogel, H., Kleffmann, J. and Kurtenbach, R.: Measured and simulated vertical profiles of nitrous acid - Part II. Model simulations and indications for a photolytic source, Atmos. Environ., 37(21), 2957–2966, doi:10.1016/S1352-2310(03)00243-7, 2003.

850 Volkamer, R., Sheehy, P., Molina, L. T. and Molina, M. J.: Oxidative capacity of the Mexico City atmosphere – Part 1: A radical source perspective, Atmos. Chem. Phys., 10(14), 6969–6991, doi:10.5194/acp-10-6969-2010, 2010.

Wang, J., Sun, S., Zhang, C., Xue, C., Liu, P., Zhang, C., Mu, Y., Wu, H., Wang, D., Chen, H. and Chen, J.: The pollution levels, variation characteristics, sources and implications of atmospheric carbonyls in a typical rural area of North China Plain during winter, J. Environ. Sci., 95, 256–265, doi:10.1016/j.jes.2020.05.003, 2020.

855 Wang, X., Wang, H., Xue, L., Wang, T., Wang, L., Gu, R., Wang, W., Tham, Y. J., Wang, Z., Yang, L., Chen, J. and Wang, W.: Observations of N$_2$O$_5$ and ClNO$_2$ at a polluted urban surface site in North China: High N$_2$O$_5$ uptake coefficients and low ClNO$_2$ product yields, Atmos. Environ., 156(3), 125–134, doi:10.1016/j.atmosenv.2017.02.035, 2017.

Wang, X., Dalton, E. Z., Payne, Z. C., Perrier, S., Riva, M., Raff, J. D. and George, C.: Superoxide and Nitrous Acid Production from Nitrate Photolysis Is Enhanced by Dissolved Aliphatic Organic Matter, Environ. Sci. Technol. Lett., 8(1), 860 53–58, doi:10.1021/acs.estlett.0c00806, 2021.

Wang, Y., Dörner, S., Donner, S., Böhnke, S., De Smedt, I., Dickerson, R. R., Dong, Z., He, H., Li, Z., Li, Z., Li, D., Liu, D., Ren, X., Theys, N., Wang, Y., Wang, Z., Xu, H., Xu, J. and Wagner, T.: Vertical profiles of NO$_2$, SO$_2$, HONO, HCHO, CHOCHO and aerosols derived from MAX-DOAS measurements at a rural site in the central western North China Plain and their relation to emission sources and effects of regional transport, Atmos. Chem. Phys., 19(8), 5417–5449, doi:10.5194/acp-865 19-5417-2019, 2019.

Whalley, L. K., Slater, E. J., Woodward-Massey, R., Ye, C., Lee, J. D., Squires, F., Hopkins, J. R., Dunmore, R. E., Shaw, M., Hamilton, J. F., Lewis, A. C., Mehra, A., Worrall, S. D., Bacak, A., Bannan, T. J., Coe, H., Percival, C. J., Ouyang, B., Jones, R. L., Crilley, L. R., Kramer, L. J., Bloss, W. J., Vu, T., Kotthaus, S., Grimmond, S., Sun, Y., Xu, W., Yue, S., Ren, L., Acton, W. J. F., Hewitt, C. N., Wang, X., Fu, P. and Heard, D. E.: Evaluating the sensitivity of radical chemistry and 870 ozone formation to ambient VOCs and NO$_x$ in Beijing, Atmos. Chem. Phys., 21(3), 2125–2147, doi:10.5194/acp-21-2125-2021, 2021.

Wild, R. J., Dubé, W. P., Aikin, K. C., Eilerman, S. J., Neuman, J. A., Peischl, J., Ryerson, T. B. and Brown, S. S.: On-road measurements of vehicle NO_2/NO_x emission ratios in Denver, Colorado, USA, Atmos. Environ., 148, 182–189, doi:10.1016/j.atmosenv.2016.10.039, 2017.

875 Wolfe, G. M., Marvin, M. R., Roberts, S. J., Travis, K. R. and Liao, J.: The framework for 0-D atmospheric modeling (F0AM) v3.1, Geosci. Model Dev., 9(9), 3309–3319, doi:10.5194/gmd-9-3309-2016, 2016.

Wong, K. W., Tsai, C., Lefer, B., Haman, C., Grossberg, N., Brune, W. H., Ren, X., Luke, W. and Stutz, J.: Daytime HONO vertical gradients during SHARP 2009 in Houston, TX, Atmos. Chem. Phys., 12(2), 635–652, doi:10.5194/acp-12-635-2012, 2012.

880 Wong, K. W., Tsai, C., Lefer, B., Grossberg, N. and Stutz, J.: Modeling of daytime HONO vertical gradients during SHARP 2009, Atmos. Chem. Phys., 13(7), 3587–3601, doi:10.5194/acp-13-3587-2013, 2013.

Wu, Z., Hu, M., Lin, P., Liu, S., Wehner, B. and Wiedensohler, A.: Particle number size distribution in the urban atmosphere of Beijing, China, Atmos. Environ., 42(34), 7967–7980, doi:10.1016/j.atmosenv.2008.06.022, 2008.

Xing, C., Liu, C., Hu, Q., Fu, Q., Wang, S., Lin, H., Zhu, Y., Wang, S., Wang, W., Javed, Z., Ji, X. and Liu, J.: Vertical 885 distributions of wintertime atmospheric nitrogenous compounds and the corresponding OH radicals production in Leshan, southwest China, J. Environ. Sci., 105, 44–55, doi:10.1016/j.jes.2020.11.019, 2021.

Xue, C., Ye, C., Zhang, Y., Ma, Z., Liu, P., Zhang, C., Zhao, X., Liu, J. and Mu, Y.: Development and application of a twin open-top chambers method to measure soil HONO emission in the North China Plain, Sci. Total Environ., 659, 621–631, doi:10.1016/j.scitotenv.2018.12.245, 2019.

890 Xue, C., Zhang, C., Ye, C., Liu, P., Catoire, V., Krysztofiak, G., Chen, H., Ren, Y., Zhao, X., Wang, J., Zhang, F., Zhang, C., Zhang, J., An, J., Wang, T., Chen, J., Kleffmann, J., Mellouki, A. and Mu, Y.: HONO Budget and Its Role in Nitrate Formation in the Rural North China Plain, Environ. Sci. Technol., 54(18), 11048–11057, doi:10.1021/acs.est.0c01832, 2020.

Xue, C., Ye, C., Kleffmann, J., Zhang, C., Catoire, V., Bao, F., Mellouki, A., Xue, L., Chen, J., Lu, K., Zhao, Y., Liu, H., Guo, Z. and Mu, Y.: Atmospheric Measurements at the Foot and the Summit of Mt. Tai – Part I: HONO Formation and Its 895 Role in the Oxidizing Capacity of the Upper Boundary Layer, Atmos. Chem. Phys. Discuss., 2021, 1–26, doi:10.5194/acp-2021-529, 2021a.

Xue, C., Ye, C., Kleffmann, J., Zhang, W., He, X., Liu, P., Zhang, C., Zhao, X., Liu, C., Ma, Z., Liu, J., Wang, J., Lu, K., Catoire, V., Mellouki, A. and Mu, Y.: Atmospheric Measurements at the Foot and the Summit of Mt. Tai – Part II: HONO Budget and Radical ($RO_x + NO_3$) Chemistry in the Lower Boundary Layer, Atmos. Chem. Phys. Discuss., 2021, 1–36, 900 doi:10.5194/acp-2021-531, 2021b.

Xue, C., Ye, C., Zhang, C., Catoire, V., Liu, P., Gu, R., Zhang, J., Ma, Z., Zhao, X., Zhang, W., Ren, Y., Krysztofiak, G., Tong, S., Xue, L., An, J., Ge, M., Mellouki, A. and Mu, Y.: Evidence for Strong HONO Emission from Fertilized Agricultural Fields and its Remarkable Impact on Regional O 3 Pollution in the Summer North China Plain, ACS Earth Sp. Chem., 5(2), 340–347, doi:10.1021/acsearthspacechem.0c00314, 2021c.

905 Xue, L. K., Wang, T., Zhang, J. M., Zhang, X. C., Deliger, Poon, C. N., Ding, A. J., Zhou, X. H., Wu, W. S., Tang, J., Zhang, Q. Z. and Wang, W. X.: Source of surface ozone and reactive nitrogen speciation at Mount Waliguan in western China: New insights from the 2006 summer study, J. Geophys. Res. Atmos., 116(7), D07306, doi:10.1029/2010JD014735, 2011.

Yang, Q., Su, H., Li, X., Cheng, Y., Lu, K., Cheng, P., Gu, J., Guo, S., Hu, M., Zeng, L., Zhu, T. and Zhang, Y.: Daytime
910 HONO formation in the suburban area of the megacity Beijing, China, Sci. China Chem., 57(7), 1032–1042, doi:10.1007/s11426-013-5044-0, 2014.

Ye, C., Liu, P., Ma, Z., Xue, C., Zhang, C., Zhang, Y., Liu, J., Liu, C., Sun, X. and Mu, Y.: High H_2O_2 Concentrations Observed during Haze Periods during the Winter in Beijing: Importance of H_2O_2 Oxidation in Sulfate Formation, Environ. Sci. Technol. Lett., 5(12), 757–763, doi:10.1021/acs.estlett.8b00579, 2018a.

915 Ye, C., Zhou, X., Pu, D., Stutz, J., Festa, J., Spolaor, M., Tsai, C., Cantrell, C., Mauldin III, R. L., Weinheimer, A., Hornbrook, R. S., Apel, E. C., Guenther, A., Kaser, L., Yuan, B., Karl, T., Haggerty, J., Hall, S., Ullmann, K., Smith, J. and Ortega, J.: Tropospheric HONO distribution and chemistry in the southeastern US, Atmos. Chem. Phys., 18(12), 9107–9120, doi:10.5194/acp-18-9107-2018, 2018b.

Zhang, J., An, J., Qu, Y., Liu, X. and Chen, Y.: Impacts of potential HONO sources on the concentrations of oxidants and
920 secondary organic aerosols in the Beijing-Tianjin-Hebei region of China, Sci. Total Environ., 647, 836–852, doi:10.1016/j.scitotenv.2018.08.030, 2019a.

Zhang, J., Chen, J., Xue, C., Chen, H., Zhang, Q., Liu, X., Mu, Y., Guo, Y., Wang, D., Chen, Y., Li, J., Qu, Y. and An, J.: Impacts of six potential HONO sources on HO_x budgets and SOA formation during a wintertime heavy haze period in the North China Plain, Sci. Total Environ., 681, 110–123, doi:10.1016/j.scitotenv.2019.05.100, 2019b.

925 Zhang, L., Wang, T., Zhang, Q., Zheng, J., Xu, Z. and Lv, M.: Potential sources of nitrous acid (HONO) and their impacts on ozone: A WRF-Chem study in a polluted subtropical region, J. Geophys. Res. Atmos., 121(7), 3645–3662, doi:10.1002/2015JD024468, 2016.

Zhang, Q., Streets, D. G., Carmichael, G. R., He, K. B., Huo, H., Kannari, A., Klimont, Z., Park, I. S., Reddy, S., Fu, J. S., Chen, D., Duan, L., Lei, Y., Wang, L. T. and Yao, Z. L.: Asian emissions in 2006 for the NASA INTEX-B mission, Atmos.
930 Chem. Phys., 9(14), 5131–5153, doi:10.5194/acp-9-5131-2009, 2009.